# A Disulfide Stabilized β-Sandwich Defines the Structure of a New Cysteine Framework M-Superfamily Conotoxin

**ARTICLE** *in* ACS CHEMICAL BIOLOGY · MAY 2015

Impact Factor: 5.33 · DOI: 10.1021/acschembio.5b00226 · Source: PubMed



**6 AUTHORS**, INCLUDING:

Aswani Kumar Kancherla

Indian Institute of Science

**3** PUBLICATIONS **18** CITATIONS

SEE PROFILE

Srinu Meesala

Indian Institute of Science Education and Re…

**1** PUBLICATION **0** CITATIONS

SEE PROFILE

Ramasamy Palanisamy

Indian Institute of Science

**1** PUBLICATION **0** CITATIONS

SEE PROFILE

Article

# A disulfide stabilized #-sandwich defines the structure of a new cysteine framework M-superfamily conotoxin

Aswani Kumar Kancherla, Srinu Meesala, Pooja Jorwal, Ramasamy Palanisamy, Sujit Kumar Sikdar, and Siddhartha Peddibhotla Sarma

*ACS Chem. Biol.*, **Just Accepted Manuscript** • DOI: 10.1021/acschembio.5b00226 • Publication Date (Web): 11 May 2015

# A disulfide stabilized β–sandwich defines the structure of a new cysteine framework M–superfamily conotoxin[#]

Aswani K. Kancherla, Srinu Meesala, Pooja Jorwal, Ramasamy Palanisamy, Sujit K. Sikdar[*] and Siddhartha P. Sarma[*]

Molecular Biophysics Unit, Indian Institute of Science, Bangalore–560012, India.

[*] Address correspondence to

e–mail: sidd@mbu.iisc.ernet.in

or

sks@mbu.iisc.ernet.in

# This manuscript is dedicated to the memory of Prof. K. S. Krishnan

**Abstract**

The structure of a new cysteine framework (--C---CC---C---C---C--) "M"– superfamily conotoxin, Mo3964, shows it to have a β–sandwich structure that is stabilized by inter–sheet cross disulfide bonds. Mo3964 decreases outward $K^+$ currents in rat Dorsal Root Ganglion neurons and increases the reversal potential of the $Na_V1.2$ channels. The structure of Mo3964 (PDB ID: 2MW7) is constructed from the disulfide connectivity pattern, i.e. 1–3, 2–5 and 4–6, that is hitherto undescribed for the "M"–superfamily conotoxins. The tertiary structural fold has not been described for any of the known *conus* peptides. NOE (549), dihedral angle (84) and hydrogen bond (28) restraints, obtained by measurement of $^{h3}J_{NC'}$ scalar couplings, were used as input for structure calculation. The ensemble of structures showed a backbone Root Mean Square Deviation of 0.68 ± 0.18 Å, with 87% and 13% of the backbone dihedral (ϕ, ψ) angles lying in the most favoured and additional allowed regions of the Ramachandran map. The conotoxin Mo3964, represents a new bioactive peptide fold that is stabilized by disulfide bonds and adds to the existing repertoire of scaffolds that can be used to design stable bioactive peptide molecules.

Natural combinatorial peptide libraries such as those expressed in the venom of predatory animals are sources of therapeutic peptides as well as lead material for drug development(*1*). Of these, the *Conus* peptides, produced by venomous marine cone snails, are noteworthy for their sequence, structural and functional diversity(*2, 3*). Two fundamental properties of these molecules have led to their emergence as drugs or drug leads, *i.e.*, functional selectivity and structural stability. These bioactive peptides have a far greater selectivity than the conventional "Small molecule" drugs (< 500 Da) and they have greater stability than the "Biologics" (> 5000 Da)(*1*). In general, bioactive peptides from venom of animals are cysteine rich and the multiple disulfide bonds reinforce the stability. Another aspect of the structure and stability of these molecules that has emerged, has been their use as structural scaffolds upon which peptides with new functionality have been designed(*4-6*).

As of date ~ 2100 conotoxins, categorized into 26 structurally distinct cysteine frameworks (arrangement of cysteines in the primary structure)(*7*), have been identified either as peptides in the venom or as amino acid sequences that have been derived from transcriptome data(*8*). Tertiary structures are known for 65 wild–type conotoxins and they are representative of 10 of the 26 known cysteine frameworks. Structural diversity among the conotoxins is a combination of the cysteine framework and of the disulfide connectivity as exemplified by the "M"–superfamily conotoxins(*9*). Thus, it is necessary to study the relationships between structure and function of conotoxins that belong to the uncharacterized cysteine frameworks, given their potential to yield molecules with new structures, scaffolds(*10*) and functions.

Recently, new cysteine framework bearing conotoxins have been discovered (*11, 12*). Analyses of precursor sequences (**Supplementary Figure S–1**) firmly suggest that these peptides belong to the "M"–superfamily conotoxins. Interestingly, the cysteine framework bears

some resemblance to the "O"– and "K"–superfamily conotoxins (*3*). We report here the three dimensional solution structure and electrophysiological activity of a representative peptide, named as Mo3964, of this new cysteine framework. The structure was determined using heteronuclear double– and triple–resonance NMR methods to extract accurate information of back–bone and side–chain hydrogen bond donor–acceptor pairs and of backbone and side–chain dihedral angles. The tertiary structure of Mo3964 represents a *new structural class* that is stabilized by a novel inter–sheet disulfide connectivity pattern.

## Methods

### Subcloning, Protein Expression and Purification

The gene was amplified from the cDNA clone(*11*) and sub–cloned into a modified pET21(a)+ expression vector(*13*). The expression, isotope enrichment and purification protocols followed were the same as described earlier for the scorpion toxin BTK–2 (*14*). The details of the yields, buffer compositions and the protocols used in cloning, expression, purification, enzymatic and chemical digestion and HPLC purification of Mo3964 are provided as supporting information.

### Molecular characterization

#### Electrophysiology

The conotoxin (10 nM final concentration) Mo3964 was applied to 1 mL of the bath solution as a bolus for both the mixed voltage gated ionic current recordings and isolated sodium currents.

**Mixed voltage gated ionic currents**

Mixed whole–cell voltage gated ionic currents were recorded from medium sized rat Dorsal Root Ganglion (DRG) neurons obtained from postnatal (P5) Wistar rats as described earlier (*15*).

**Voltage gated sodium currents**

Isolated whole–cell sodium currents were recorded from the rat brain type IIA voltage gated sodium channel α–subunit (rNav1.2a), stably expressed in Chinese hamster ovary (CHO) cells(*16*). Boltzmann charge–voltage equation was used for fitting the conductance–voltage plot for each cell to show statistically significant change in $V_{1/2}$ after Mo3964 application. The details of the electrophysiology protocols are provided as supporting information.

**Chemical Modification Reactions and Mass Spectrometry**

Mass analyses of purified and of chemically modified peptides were carried out by either MALDI Mass Spectrometry (UltrafleXtreme, Bruker Daltonics, Germany) or by Electro Spray Ionization Mass Spectrometry (HCT Ultra ETD II ion trap mass spectrometer, Bruker Daltonics, Germany) connected to an Agilent 1100 series HPLC system. Disulfide connectivity was established using the protocol prescribed by Wu and Watson(*17*). The experimental details of mass spectral data acquisition, processing and protocols of the chemical modification reactions are provided as supporting information.

**Optical Spectroscopy**

Fluorescence emission and circular dichroism spectra of Mo3964 were acquired in native and denaturing conditions induced by chaotropic and/or reducing agents.

Fluorescence data was acquired on a JASCO FP–6300 spectrofluorimeter. All measurements were made on samples of Mo3964 that were 1 μM in concentration. The bandwidth for excitation and emission was 5 nm. The final spectra were averaged over three scans and were baseline corrected by subtracting the spectrum of the appropriate blank solution.

Circular Dichroism (CD) spectra were acquired on a JASCO–715 spectropolarimeter over a wavelength range of 190 to 250 nm for the far–UV CD spectra and 250 to 350 nm for the near–UV CD spectra. The CD data were acquired with a scan rate of 100 nm per minute and a data pitch of 2 per nm using a 0.2 cm path length cuvette. The final spectra were averaged over three scans, baseline corrected by subtracting the spectrum of appropriate blank solution and smoothed using a running average protocol available with the JASCO spectra analysis software.

**Analytical Size Exclusion Chromatography**

Size exclusion chromatography studies were carried out on a GE Healthcare Superdex S75 (10/300 GL) pre–packed analytical column connected to Biorad FPLC system at 4 ºC. Two hundred microliters of a 1.4 mg/ml solution of Mo3964 was injected onto the column and eluted using a flow rate of 0.5 ml per minute. The elution volumes of Mo3964 were compared with those of protein molecular weight standards. Details of the size exclusion chromatography experiments are provided as supporting information.

**Multi Angle Light Scattering (MALS)**

Light scattering data was acquired on peptide samples that were eluted from an analytical Superdex S75 column (GE Healthcare) connected to a Wyatt Treos multi–angle light scattering

instrument with an inline refractive index detector (Waters 2414 RI detector) and a multi–wavelength UV detector (Shimadzu SPD–10A VP UV–Vis detector). Approximately 100 µL of a 6.5 mg/mL protein solution was injected onto the column. The scattered light was measured at three angles (43.6°, 90.0°, 136.4°) and the molar mass was calculated by fitting the light scattering data to Zimm's model (fitting degree of 1) using the ASTRA program (Wyatt Technology).

**NMR Spectroscopy**

**Sample Preparation**

Samples for NMR spectroscopy were prepared by dissolving the lyophilized peptide either in sterile milliQ water (10% $D_2O$) or 100% $D_2O$ in 50 mM $^2H_3$–Acetate buffer (pH 5.35, uncorrected for deuterium isotope effect) containing 0.01% sodium azide. Concentration of samples ranged between 0.5 to 1.0 mM.

**Data Acquisition**

NMR data were acquired at 25 °C on a 600 MHz Agilent NMR spectrometer using a triple resonance room temperature probe or a cryogenically cooled probe fitted with a single ( z axis ) pulsed field gradient accessory. Multi–dimensional heteronuclear nmr data(*18-21*) were acquired on isotopically enriched samples of Mo3964, for establishing sequence specific resonance assignments, NOE correlations (*22*), hydrogen bond correlations(*23*), for measuring back–bone coupling constants (*24*) and side–chain $\chi^1$ dihedral angles(*25, 26*), $^{15}N$–relaxation parameters(*27*) and H/D exchange parameters(*28*). All NMR data were processed on an Intel PC work station running SuSe Linux version 11.4 using NMRPipe/NMRDraw processing software(*29*).

Processed spectra were analyzed using CcpNmr Analysis version 2.1(*30*). The list of NMR experiments, data acquisition parameters and processing protocols are described in supporting information (**Supplementary Table ST–1 and as Supplementary Methods**).

**Structural restraints and structure calculation**

**Structural restraints**

Rotation correlation time ($\tau_c$) was calculated from experimentally derived $^{15}N$ $R_1$ and $R_2$ relaxation rates.

Backbone φ and ψ dihedral angles were calculated from $^{3}J_{H}^{N}{}_{-H}^{\alpha}$ coupling constants obtained from 3D HNHA data(*24*) and from the prediction programs TALOS+(*31*) and DANGLE(*32*). Side–chain $\chi^1$ dihedral angle conformation and stereospecific assignments for the β–methylene protons were determined using the methods described by Bax et al(*33*).

Distance restraints, from peak intensities of unambiguously assigned inter–proton correlations in the $^{15}N$– and $^{13}C$–edited NOESY spectra, were generated using the 'Make Distance Restraints" routine in CcpNmr suite(*30*). An absolute maximum of 6.0 Å was set for the upper distance limit. Lower distance limits were set at 1.8 Å for all the inter proton distance restraints.

Hydrogen bond restraints were derived from H/D exchange studies and by identification of correlations in the Long–Range HNCO experiment. H/D exchange studies were carried out by acquisition of series of $^{1}H,^{15}N$–HSQC spectra. Amide protons that were not exchanged up to eleven hours in the H/D exchange study were considered to be either buried or involved in a stable hydrogen bond(*28*). The hydrogen bond restraints were included as distance of acceptor oxygen from the donor nitrogen and proton with upper limits of 3.5 Å and 2.5 Å respectively.

Restraints for disulfide bond between two cysteines $Cys_i$ and $Cys_j$ were included as distances

between $S^{\gamma}_{i}$–$S^{\gamma}_{j}$, $C^{\beta}_{i}$–$S^{\gamma}_{j}$ and $S^{\gamma}_{i}$–$C^{\beta}_{j}$ atoms with both the upper and lower limits at 2.05 Å, 3.05 Å and 3.05 Å respectively. For all the pairs of sulphur atoms which are not involved in disulfide bond with each other, an explicit lower distance limit of 3.5 Å was included.

Structures were calculated using CYANA(*34*) and refined using CNS(*35*). The details of the structure calculation and refinement protocols are given in the Supplementary Methods. Structures were analysed using MOLMOL(*36*) and UCSF Chimera(*37*).

## Results and Discussion

The purified Mo3964 peptide elutes as a single disulfide foldamer peak in RP–HPLC (**Figure 1a**) and its mass exactly matches the calculated mass (**Figure 1b** and **Supplementary Figure S–2)**. Alkylation of Mo3964 in the presence and absence of reducing agents (**Supplementary Figure S–3**) shows that the cysteines in Mo3964 are oxidized.

The Mo3964 peptide exhibits positive ellipticity in the far–UV region of the CD spectrum (**Figure 1c**). Such spectral properties are also exhibited by oxidized ω–GVIA (a member of the "O"–superfamily of conotoxins which are known to adopt the ICK–motif), for which the observed positive ellipticity was attributed to a sterically constrained aromatic amino acid. Replacement of this aromatic amino acid resulted in loss of this spectral feature (*38*). We show below that despite the similarity in the CD spectrum, Mo3964 does not adopt an ICK motif fold. The spectrum, when recorded under reducing conditions resembles that of an unfolded protein with a characteristic minimum at about 195 nm.

Fluorescence emission studies of oxidized and reduced Mo3964, under native and denaturing conditions (**Figure 1d**) showed that no visible change is observed in the absence of a reducing

agent. The emission maximum remained unperturbed even in the presence of chaotropic agents (7M Urea and 6M Guanidinium chloride). A red shift in the emission spectral line (340 nm to 349 nm) upon reduction indicates that the single tryptophan in Mo3964 is buried in the native peptide.

Multi–angle light scattering (MALS) data (**Figure 1e**) and rotational correlation time ($\tau_c$) of 2.3 ns calculated using $^{15}$N–relaxation data (**Figure 1f and Supplementary Figure S–4**) unambiguously indicate that Mo3964 exists as a monomer in solution.

## Electrophysiology

### Mixed voltage gated ionic currents

The medium sized DRG neurons showed both inward and outward currents in response to depolarizing voltage steps (**Figure 2a**). Bolus application of Mo3964 preferentially reduced the outward currents that are due to the opening of voltage gated $K^+$ channels. This is indicated by the current traces shown in **figures 2a (i)–(iii)** and the I–V plot shown in **figure 2a (iv)**.

The effect of Mo3964 on isolated inward voltage gated sodium currents (**figures 2b (i),(ii)**) show that it did not alter the time course of the sodium currents. A decrease in the outward $Na^+$ currents was observed in the recordings at higher potential steps. This also manifests as a decrease in the peak current amplitudes at potentials positive to +30 mV in the I–V plot. A shift in $E_{rev}$ by +8 mV (control: 53.50 mV ± 2.98 mV and Mo3964: 61.64 ± 2.70 mV; $p<0.05$, two–tailed paired t–test), when compared to the control was observed in the presence of Mo3964 (**Figure 2b (iii)**). The averaged normalized conductance–voltage plot (**Figure 2b (iv)**) shows the leftward shift in the presence of Mo3964, as also seen in the current–voltage plot (**Figure 2b**

**(iii)**). The data were fit to the Boltzmann charge–voltage equation (Equation 3 in Supporting Information) and the change in $V_{1/2}$ following application of Mo3964 was found to be statistically significant (control: 10.9 ± 2.30 mV and Mo3964: 13.05 ± 2.32 mV; $p<0.05$, two–tailed paired t–test). A rightward shift in the reversal potential implies an increase in the permeability of the voltage gated sodium channels to $Ca^{2+}$ ions and loss of selectivity for $Na^{+}$. A leftward shift in the conductance–voltage plot indicates an increase in the voltage sensitivity of the channel. From these preliminary experiments it may be concluded that Mo3964 affects the voltage sensor and the selectivity filter components of the voltage gated sodium channels. Animal toxins have been shown to target multiple ion channel types (*39-41*). It has been hypothesized that multiple channel activities exhibited by a specific animal toxin, suggests common interaction sites between distantly related ion channels or receptors (*42*).

## Solution structural studies of Mo3964

### *Sequence Specific Resonance Assignments*

Sequence specific resonance assignments were obtained from a standard suite of heteronuclear double– and triple–resonance NMR spectra (**Supplementary Table ST–1**). Strip plots from 3D HNCACB(*43*) and CBCACONH(*44*) spectra show sequential correlations for residues $Trp^{25}$ to $Asn^{36}$ (**Supplementary Figure S–5).** Backbone $^{15}N–H^{N}$ correlations in the $^{1}H,^{15}N$–HSQC spectrum (**Figure 3a**) were observed for all the residues except $Lys^{7}$. Assignments for $Lys^{7}$ were obtained from other inter–residue correlations. The $^{13}C^{\beta}$ chemical shifts of the six cysteines varied between 39 to 47 ppm range (**Figure 3b**) and are characteristic of oxidized cysteines(*45*). The protons of $Lys^{7}$ and $Pro^{24}$ exhibited strikingly up–field chemical shift values, when

compared to other lysine and proline residues within Mo3964. The anomalous chemical shift values of these protons (**Supplementary Table ST–2)** could only arise due to their spatial proximity to the sole $Trp^{25}$ aromatic ring(*46*). Near complete sequence specific resonance assignments (BMRB ID 25302) are presented in the **Supplementary Table ST–3**.

**Proline *cis–trans* isomerization and conformational equilibria**

The observed $^{13}C$ $\Delta\delta_{\beta\gamma}$ values for prolines (**Figure 3c**) indicate that the $Asp^{23}$–$Pro^{24}$ peptide bond is in cis conformation ($\Delta\delta_{\beta\gamma}$ $Pro^{24}$ =10 ppm ) while $Pro^{10}$, $Pro^{15}$ and $Pro^{37}$ ($\Delta\delta_{\beta\gamma}$ is in the range of 4 to 5 ppm) are in trans conformation(*47*). It is interesting to note that ~ 3 – 4 % of the Asp–Pro peptide bonds have been found to be in the *cis* conformation (*48*). Doubling of the amide proton resonances seen in the HSQC (**cf. Figure 3a**) results from the conformational equilibrium due to cis–trans isomerization about the $Asp^{23}$–$Pro^{24}$ peptide bond and these two conformers were in slow exchange on the chemical shift time scale. Assignments for the minor form could be obtained for the amide proton resonances of $Gly^2$, $Glu^3$, $Cys^4$, $Gly^5$, $Asp^6$, $Glu^9$, $Asn^{22}$, $Asp^{23}$, $Trp^{25}$, $Ile^{28}$, $Asn^{36}$ and the $H^{\varepsilon}$ of the $Trp^{25}$ side chain.

**Coupling constants, dihedral angles and stereospecific assignments**

The $^3J_H{}^N{}_H{}^{\alpha}$ coupling constants and the $\phi$ dihedral angles were determined for 27 residues(*24*). The conformation about the $C^{\alpha}$ – $C^{\beta}$ bond (dihedral angle $\chi^1$) and stereospecific assignment for the β–methylene protons were obtained for 19 residues(*33*). **Figure 4** shows strip plots from 3D–HNHB(*25*) and HNCOHB spectra (*26*). It can be seen that $Cys^{27}$ is the only residue whose side chain was found to be in $g^2t^3$ ($\chi^1$ = 180°) conformation. Ten residues viz., $Glu^3$, $Cys^4$, $Cys^{11}$,

Cys[12], Asp[16], Asn[22], Asp[23], Ser[31], Ser[32] and Arg[33] have $\chi^1$ angles in the $g^2g^3$ (+60°) conformation while eight residues viz., Asp[6], Asp[8], Arg[14], Lys[19], Cys[21], Trp[25], Leu[29] and Cys[34] have $\chi^1$ angles in $t^2g^3$ (–60°) conformation.

**NOESY Assignments**

**Sequential and medium–range NOESY correlations**

Sequential NOE correlations ($H^{\alpha}_{i}$ to backbone $H^{N}_{i+1}$ or $H^{\delta}_{i+1}$ in the case of proline) corroborated the sequence specific assignments obtained from triple resonance NMR data. The sequential NOE correlations for residues Trp[25] to Asn[36] are shown in **Supplementary Figure S–6**. The $H^{\alpha}_{i}$ to $H^{\delta}_{i+1}$ and $H^{N}_{i}$ to $H^{\delta}_{i+1}$ NOESY correlations, were observed across the Xxx–Pro[10], Pro[15] and Pro[37] trans peptide bonds respectively. A sequential $H^{\alpha}$–$H^{\alpha}$ NOE correlation, across the *cis* Asp[23]–Pro[24] peptide bond could not be assigned due to resonance overlap of the $H^{\alpha}$ nuclei of these residues. The absence of unique NOE correlations for the minor conformer precluded the determination of its structure.

**Secondary structure of Mo3964**

Based on the pattern of NOEs, coupling constants and chemical shifts **(Figure 5)** residues 9–10, 12–14, 19–21, 26–28 and 33–35 are in an extended, β–strand like conformation (labelled as β1 to β5). Residues 1–3, are present in a "random–coil" conformation. Loops 2 (residues 14–18) and 3 (residues 22–25) form type 1β and type VIa turns. Loop 1 (residues 4–8) bridges residues Cys[4] and Glu[9] and loop 4 (residues 29–32) bridges residues in β4 and β5. Residues Asn[36] and Pro[37], at the C–terminus are also in an extended conformation.

**Long–range correlations and topology**

A significant proportion (~ 27%) of the total NOE correlations assigned are long range correlations (**Table 1**). NOE correlations between the side chains of $Trp^{25}$ and $Lys^{7}$ ($H^{\varepsilon}$ of $Trp^{25}$ to $H^{\alpha}$, $H^{\beta2}$ and $H^{\beta3}$ of $Lys^{7}$) establish the spatial proximity of these residues **(Figure 6a)**, thereby substantiating the ring–current effect as the cause of up–field shifted values observed for $H^{\alpha}$, $H^{\beta2}$ and $H^{\beta3}$ of $Lys^{7}$. Presence of characteristic long–range backbone to backbone correlations ( $H^{N}\rightarrow H^{N}$, $H^{N}\rightarrow H^{\alpha}$) (**Supplementary Figure S–6**) indicate that β2–loop2–β3 and β4–loop4–β5 form two pairs of anti–parallel beta–strands separated by reverse turns.

Solvent exchange ($H_2O/D_2O$) studies showed that the backbone amide protons of thirteen residues viz., $Gly^{5}$, $Asp^{6}$, $Asp^{8}$, $Glu^{9}$, $Cys^{11}$, $Cys^{12}$, $Asn^{22}$, $Trp^{25}$, $Val^{26}$, $Ile^{28}$, $Arg^{33}$, $Cys^{34}$, and $Glu^{35}$ were slow to exchange (protected up to 11 hours). $Asp^{6}$, $Asp^{8}$ and $Cys^{11}$ exchanged shortly thereafter, and the remaining amide protons listed above were un–exchanged even after 192 hours.

Long–range scalar couplings (**Supplementary Table ST–4**) were obtained for 14 HN and CO hydrogen–bond donor–acceptor pairs(*23*) (**Figure 6b**). No correlations were observed for $Asn^{22}$ and $Trp^{25}$. The $^{h3}J_{NC'}$ hydrogen bond correlations between $Val^{20} \rightarrow Cys^{12}$ and $Arg^{14} \rightarrow Ala^{18}$, between $Val^{26} \leftrightarrow Glu^{35}$ and $Ile^{28} \rightarrow Arg^{33}$ and between $Cys^{34} \leftrightarrow Glu^{9}$ unequivocally established the registry between strands β2 and β3, β4 and β5, and β5 and β1 **(Figure 6c)** respectively. *The long–range HNCO experiment proved to be an extremely crucial experiment, data from which enabled determination of the structural topology with the highest degree of confidence.* **Figure 6c (inset)** shows the secondary structure topology derived from experimentally observed long range backbone NOE and hydrogen bond correlations. Hydrogen bond correlations were also

observed to the backbone amide proton–nitrogen pairs of $Asp^{6}$, $Asp^{8}$, $Asp^{23}$ and $Asn^{36}$, the acceptor group for which was assumed to be the side–chain carbonyl groups of these amino acids(*49*).

**Determination of disulfide connectivity**

Among the conotoxins, the most common disulfide connectivity, i.e., 1–4, 2–5 and 3–6, is observed among members of the "O"–superfamily(*7*) and the M–4 and M–5 branches of the "M"–superfamily(*9, 50*). The "mini"–M conotoxins show the cysteine pairing 1–5, 2–4 and 3–6 for the M–1 branch conotoxins(*51*) and 1–6, 2–4 and 3–5 for the M–2 branch conotoxins(*52*) respectively. A rare instance of the sequential cysteine pairing, i.e., 1–2, 3–4 and 5–6 has been proposed for Im23a(*10*), a member of the "K"–superfamily. From the studies above, it is clear that the molecular topology of Mo3964 is one that has not been observed among three–disulfide conotoxins and therefore assignment of disulfide connectivity by homology is imprudent. Determination of the disulfide connectivity was an important component of the structure determination process in this study.

**Cyanylation and chemical cleavage**

Disulfide connectivity in Mo3964 was established by partial reduction, cyanylation followed by alkali mediated chemical cleavage(*17*). This method can be employed where other disulfide determination methods such as direct MS fragmentation of intact molecules(*53*) or partial reduction and alkylation(*54*) fail. The chemical mechanism and method of analysis are given in **Supplementary Figure S–7**. HPLC chromatograph **(Figure 7a)** of Mo3964 after partial reduction and cyanylation shows that the partially reduced and cyanylated molecules elute from

the 56th minute onwards. MALDI–MS revealed that fractions 14 to 16a **(Figure 7b)** consist predominantly of the singly reduced and cyanylated species, while fractions 17 and 18 are mixtures of singly and higher order cyanylated species **(Supplementary Figure 8a)**.

**Analysis of peptide fragments from fractions 14a, 15, 16 and 16a**

Two peptide ions of m/z 323.8 and 2845.5 were observed from base mediated cleavage of singly reduced and cyanylated Mo3964 from the fractions 14a, 15, 16 and 16a **(Figures 7c,d)**. The ion of m/z 2845.5 corresponds to the peptide $Cys^{12}$ to $Pro^{37}$, indicating that $Cys^{12}$ is disulfide bonded to either $Cys^{4}$ or $Cys^{11}$. The ion at m/z 323.8 corresponds to the N–terminal fragment ($Asp^{1}$ to $Glu^{3}$) obtained upon cleavage of the $Glu^{3}$–$Cys^{4}$ peptide bond. *This is conclusive proof that $Cys^{4}$ was reduced along with $Cys^{12}$, and they are disulfide paired.*

Therefore, there are three possible disulfide bond combinations between the remaining four cysteines. The list of expected peptide fragments for the three remaining disulfide connectivities are listed in **Supplementary Table ST–5**.

Analysis of peptide fragments in fraction 17 proved to be difficult due to the multiplicity of reduced and cyanylated species. Peptide fragments at m/z 1517.8 and 1927.9 that correspond uniquely to the connectivity ($Cys^{11}$–$Cys^{27}$, $Cys^{21}$–$Cys^{34}$) were observed **(Supplementary Figures S–8b–d).** Importantly, unique fragments that correspond to the remaining two connectivities were not observed. Thus the data strongly suggests that the disulfide pairing in Mo3964 is $Cys^{4}$–$Cys^{12}$; $Cys^{11}$–$Cys^{27}$; $Cys^{21}$–$Cys^{34}$. However, given the complex nature of the mixture in fraction 17, additional evidence for the disulfide bonds $Cys^{11}$–$Cys^{27}$; $Cys^{21}$–$Cys^{34}$ was sought.

**NMR spectroscopy**

Comparison of HNHB and HN(CO)HB NMR data (*33*) showed that χ1 dihedral angles for the six cysteine residues (cf. **Figure 4**) in ascending order of sequence number was +60°, +60°, +60°, –60°, 180°, –60° respectively. Pairs of disulfide bonded cysteines present in the non–hydrogen bonded registry in anti–parallel beta sheets have $\chi^1$ values around –60°(*55*). Thus $Cys^{27}$ and $Cys^{34}$ (**cf. Figure 6c**) are unlikely to be disulfide paired. $Cys^{27}$ could disulfide pair with $Cys^{11}$ or $Cys^{21}$, thereby reducing the number of possible disulfide combinations from 15 to 2 (**Figure 8a**). Initial structures were calculated without disulfide bond restraints and these restraints along with χ1 angle restraints were imposed during the later stages of structure calculation. The disulfide connectivity in the resulting three dimensional structures, that was consistent with the NMR and mass spectrometric data, was $Cys^4$–$Cys^{12}$, $Cys^{11}$–$Cys^{27}$ and $Cys^{21}$–$Cys^{34}$. *It is noteworthy that the cysteine framework in Mo3964 is novel and that this disulfide pairing pattern is unprecedented among the "M"–superfamily conotoxins (7).*

**Tertiary structure of Mo3964**

**Table 1** lists the number and type of all restraints used for structure determination and the structural statistics. **Figure 8b** shows the stereo view of the overlay of the backbone atoms of the best 20 structures selected after refinement. The ensemble of structures has a backbone and all heavy atom Root Mean Square Deviation of 0.68 ± 0.18Å and 1.18 ± 0.16Å respectively. Ramachandran analysis(*56, 57*) of the ensemble of structures reveals that 87.7% and 12.3% of the residues have backbone dihedral angles that lie in the most favoured region and additional allowed regions of the map (**Supplementary Figure S–9**).

Tertiary structure of Mo3964 shows that the strands β1 and β2 are formed by residues $Glu^{9}$ to $Arg^{14}$ with a break at $Cys^{11}$ (**Figures 6c and 8c**). $Cys^{11}$ acts as a pivot, and its conformation causes a significant change in the plane and direction of the peptide backbone. This change enables residues $Glu^{9}$ and $Pro^{10}$ (strand β1) to interact with strand β5 and residues $Cys^{12}$ to $Arg^{14}$ (strand β2) to interact with strand β3. The beta strands β1, β4 and β5 form the first anti–parallel three–stranded beta sheet while the strands β2 and β3 form the second anti–parallel two–stranded beta sheet. Loop 3 (a type VIa turn) connects these beta sheets. The two beta sheets are folded back such that C–terminal strand β5 loops back to interact with the N–terminal strand β1 giving the structure the appearance of a *β–sandwich* that is stabilized by two disulfide bonds in the core of the molecule. **Figure 9a** shows the side and top view of the structural core of Mo3964 and the inter–sheet NOE correlations (**Supplementary Figure S–10**) which define the disulfide bonded β–sandwich structure.

The aromatic ring of $Trp^{25}$ is packed in by the side chains of the residues $Asp^{6}$, $Lys^{7}$, $Asn^{22}$, $Pro^{24}$, $Asn^{36}$ and $Pro^{37}$. These interactions further stabilize this end of the β–sandwich structure. In particular, the aliphatic side chains of $Lys^{7}$ and $Pro^{24}$ tightly sandwich the indole ring of $Trp^{25}$ and hence show maximum perturbation in the proton chemical shifts due to the ring current effect. **Figure 9b** shows the CH•••π interactions between the aromatic ring of $Trp^{25}$ and the side chains of $Lys^{7}$ and $Pro^{24}$. The backbone amide protons of $Asn^{22}$ and $Trp^{25}$, which did not show long–range h–bond correlations, were found to be within hydrogen bonding distance of $Gly^{5}CO$ (N•••O 3.0 Å, H-N-O 14°) and $Asn^{22}CO$ (N•••O 2.9 Å, H-N-O 34°) respectively. The latter hydrogen bond stabilizes the Type VI reverse turn in loop 3.

**Disulfide bond geometry**

Accessible surface area (ASA) calculations show that $Cys^{4}$ (ASA 20.5) and $Cys^{12}$ (ASA 18.8) are solvent exposed, while cysteines 11, 21, 27 and 34 have percentage ASAs of 6.9, 12.7, 3.4 and 0.0 respectively and are considered to be buried. The percentage ASAs for the sulphur atoms of the latter set are still lower. The disulfide bonds $Cys^{11}$–$Cys^{27}$ and $Cys^{21}$–$Cys^{34}$ cross link the two–stranded and the three stranded beta sheets. These disulfide bonds appear to run across each other forming a veritable "Gordian Knot" (**Figures 8b,c**).

**Structure and stability**

In Mo3964, there exists an intricate relationship between the disulfide connectivity, disulfide geometry, tertiary structure and the stability of the molecule. The inter–sheet cross disulfide geometry provides the foundation for the extreme stability of Mo3964 towards temperature, denaturation by chaotropic agents and resistance to proteolysis. Fluorescence (cf. **Figure 1d**) and NMR spectroscopy (**Figures 9c**) show that Mo3964 denatures only when disulfides are reduced to thiols. The striking C-H•••π interactions between the $Lys^{7}$ side chain protons and the $Trp^{25}$ aromatic ring were unperturbed in all but the reducing conditions tested here. As in the case of ω–GVIA, the rigid conformation of the $Trp^{25}$ aromatic ring may be the source of the anomalous positive ellipticity observed in the CD spectrum of Mo3964 (*38*).

The other disulfide connectivities (cf. **Figure 8a**) considered during structure calculation would have resulted in structures with lower stability towards chemical denaturation even in the absence of reducing agents.

A DALI(*58*) search showed that Mo3964 has no structural relative. The structure of Mo3964

bears very little resemblance to the widely distributed three disulfide conotoxins of the "O"–superfamily *viz*., ω, δ and κ–conotoxins, all of which bear the "inhibitory cysteine knot" fold (*5, 59*). Mo3964 does not possess this fold despite the resemblance in the cysteine framework. Although the precursor sequence of Mo3964 resembles that of the M–1 branch of the "M"–superfamily of conotoxins (*9*), it is clear that Mo3964 exhibits a unique cysteine framework, disulfide connectivity and tertiary structure. The potency of Mo3964 in modulating neuronal sodium and potassium ion currents, provides an unique opportunity for the design of peptides, on this novel scaffold, to separate out structural features responsible for these activities. Wommack and co–workers have recently reported the structure of HD5–CD, a disulfide locked $C_2$–symmetric defensin peptide (*60*). This structure is stabilized by inter–subunit disulfide bonds. *The structural architecture of Mo3964 is similar to the beta–barrel–like core formed by two beta sheets that belong to separate chains in the dimeric HD5–CD. The most significant difference lies in the fact that Mo3964 is a monomer.* While Mo3964 resembles the β–sandwich fold, the two β–sheets are offset when viewed in a plane parallel to the long–axis of the molecule. The shape anisotropy of Mo3964 is also reflected in its analytical gel–filtration retention factor which is similar to that of a larger globular protein of size 8 kDa (**Supplementary Figure S–11).**

In conclusion, the three dimensional structure of Mo3964 exhibits a novel fold that has hither–to–fore not been described for any other member of this class of pharmacologically active peptides. The increasing importance of peptides as therapeutic(*61*), and / or diagnostic agents(*6*) makes the discovery of peptides with new structural attributes and new or improved functionality important. In this regard the sequence and structure of Mo3964 assumes significance, given its

novel fold, stability and solubility, and that this scaffold could be utilized for engineering new chemistries and functions.

**Acknowledgements**

The cDNA clone of Mo3964 was a kind gift from Prof. P. Balaram and Dr. Kalyan K Dewan. Authors thank Mr. Raghu Tadala and Mrs. Sunita Prakash for acquiring mass spectrometric data. AKK thanks CSIR for a senior research fellowship. DBT and DST are acknowledged for NMR and mass spectrometric facilities at the Indian Institute of Science. The authors are indebted to Late Prof. K. S. Krishnan (The National Center for Biological Sciences, Tata Institute of Fundamental Research) for his inspiration and enthusiasm and for fostering conotoxin research in India. This manuscript is dedicated to the memory of Prof. K. S. Krishnan.

**References:**


1. Craik, D. J., Fairlie, D. P., Liras, S., and Price, D. (2013) The Future of Peptide–based Drugs, *Chemical Biology & Drug Design 81*, 136–147.
2. Olivera, B. M., Rivier, J., Clark, C., Ramilo, C. A., Corpuz, G. P., Abogadie, F. C., Mena, E. E., Hillyard, D. R., and Cruz, L. J. (1990) Diversity of Conus neuropeptides, *Science 249*, 257–263.
3. Terlau, H., and Olivera, B. M. (2004) Conus venoms: a rich source of novel ion channel–targeted peptides, *Physiol Rev 84*, 41–68.
4. Barba, M., Sobolev, A. P., Zobnina, V., Bonaccorsi di Patti, M. C., Cervoni, L., Spiezia, M. C., Schinin, M. E., Pietraforte, D., Mannina, L., Musci, G., and Polticelli, F. (2012) Cupricyclins, Novel Redox–Active Metallopeptides Based on Conotoxins Scaffold, *PLoS ONE 7*, e30739.
5. Daly, N. L., and Craik, D. J. (2011) Bioactive cystine knot proteins, *Current Opinion in Chemical Biology 15*, 362–368.
6. Zoller, F., Markert, A., Barthe, P., Hebling, U., Altmann, A., Lindner, T., Mier, W., and Haberkorn, U. (2013) A Disulfide–Constrained Miniprotein with Striking Tumor–Binding Specificity Developed by Ribosome Display, *Angewandte Chemie International Edition 52*, 11760–11764.
7. Kaas, Q., Yu, R., Jin, A. H., Dutertre, S., and Craik, D. J. (2012) ConoServer: updated content, knowledge, and discovery tools in the conopeptide database, *Nucleic Acids Res 40*, D325–330.
8. Dutertre, S., Jin, A. H., Kaas, Q., Jones, A., Alewood, P. F., and Lewis, R. J. (2013) Deep venomics reveals the mechanism for expanded peptide diversity in cone snail venom, *Mol Cell Proteomics 12*, 312–329.
9. Corpuz, G. P., Jacobsen, R. B., Jimenez, E. C., Watkins, M., Walker, C., Colledge, C., Garrett, J. E., McDougal, O., Li, W., Gray, W. R., Hillyard, D. R., Rivier, J., McIntosh, J. M., Cruz, L. J., and Olivera, B. M. (2005) Definition of the M–conotoxin superfamily: characterization of novel peptides from molluscivorous Conus venoms, *Biochemistry 44*, 8176–8186.
10. Ye, M., Khoo, K. K., Xu, S., Zhou, M., Boonyalai, N., Perugini, M. A., Shao, X., Chi, C., Galea, C. A., Wang, C., and Norton, R. S. (2012) A helical conotoxin from *Conus imperialis* has a novel cysteine framework and defines a new superfamily, *J Biol Chem 287*, 14973–14983.
11. Dewan, K. K. (2007) Precursor conotoxin sequences from *Conus achatinus* and *Conus monile*, In *Molecular Biophysics Unit*, p 147, Indian Institute of Science, Bangalore.
12. Liu, Z., Li, H., Liu, N., Wu, C., Jiang, J., Yue, J., Jing, Y., and Dai, Q. (2012) Diversity and evolution of conotoxins in *Conus virgo*, *Conus eburneus*, *Conus imperialis* and *Conus marmoreus* from the South China Sea, *Toxicon 60*, 982–989.
13. Mitra, A., Chakrabarti, K. S., Shahul Hameed, M. S., Srinivas, K. V., Senthil Kumar, G., and Sarma, S. P. (2005) High level expression of peptides and proteins using cytochrome $b_5$ as a fusion host, *Protein Expr Purif 41*, 84–97.
14. Kumar, G. S., Upadhyay, S., Mathew, M. K., and Sarma, S. P. (2011) Solution structure of BTK–2, a novel hK(v)1.1 inhibiting scorpion toxin, from the eastern Indian scorpion *Mesobuthus tamulus*, *Biochim Biophys Acta 1814*, 459–469.

15. Sabareesh, V., Gowd, K. H., Ramasamy, P., Sudarslal, S., Krishnan, K. S., Sikdar, S. K., and Balaram, P. (2006) Characterization of contryphans from *Conus loroisii* and *Conus amadis* that target calcium channels, *Peptides 27*, 2647–2654.
16. Sarkar, S. N., Adhikari, A., and Sikdar, S. K. (1995) Kinetic characterization of rat brain type IIA sodium channel alpha–subunit stably expressed in a somatic cell line, *The Journal of physiology 488*, 633–645.
17. Wu, J., and Watson, J. T. (1997) A novel methodology for assignment of disulfide bond pairings in proteins, *Protein Sci 6*, 391–398.
18. Kay, L., Keifer, P., and Saarinen, T. (1992) Pure absorption gradient enhanced heteronuclear single quantum correlation spectroscopy with improved sensitivity, *Journal of the American Chemical Society 114*, 10663–10665.
19. Grzesiek, S., and Bax, A. (1992) Improved 3D triple–resonance NMR techniques applied to a 31 kDa protein, *Journal of Magnetic Resonance (1969) 96*, 432–440.
20. Bax, A., and Grzesiek, S. (1993) Methodological Advances in Protein NMR, *Acc. of Chem. Res. 26*, 131138.
21. Muhandiram, D. R., and Kay, L.E. (1994) Gradient–Enhanced TripleResonance Three–Dimensional NMR Experiments with Improved Sensitivity., *J. Magn. Reson. 193*, 203–216.
22. Marion, D., Driscoll, P. C., Kay, L. E., Wingfield, P. T., Bax, A., Gronenborn, A. M., and Clore, G. M. (1989) Overcoming the overlap problem in the assignment of $^{1}$H NMR spectra of larger proteins by use of three–dimensional heteronuclear $^{1}$H–$^{15}$N Hartmann–Hahn–multiple quantum coherence and nuclear Overhauser–multiple quantum coherence spectroscopy: application to interleukin 1 beta, *Biochemistry 28*, 6150–6156.
23. Cordier, F., Nisius, L., Dingley, A. J., and Grzesiek, S. (2008) Direct detection of N–H[•••]O=C hydrogen bonds in biomolecules by NMR spectroscopy, *Nat Protoc 3*, 235–241.
24. Vuister, G. W., and Bax, A. (1993) Quantitative J correlation: a new approach for measuring homonuclear three–bond J(HNH.alpha.) coupling constants in $^{15}$N–enriched proteins, *Journal of the American Chemical Society 115*, 7772–7777.
25. Archer, S. J., Ikura, M., Torchia, D. A., and Bax, A. (1991) An alternative 3D NMR technique for correlating backbone $^{15}$N with side chain Hβ resonances in larger proteins, *Journal of Magnetic Resonance (1969) 95*, 636–641.
26. Grzesiek, S., Ikura, M., Marius Clore, G., Gronenborn, A. M., and Bax, A. (1992) A 3D triple–resonance NMR technique for qualitative measurement of carbonyl–Hβ J couplings in isotopically enriched proteins, *Journal of Magnetic Resonance (1969) 96*, 215–221.
27. Farrow, N. A., Muhandiram, R., Singer, A. U., Pascal, S. M., Kay, C. M., Gish, G., Shoelson, S. E., Pawson, T., Forman–Kay, J. D., and Kay, L. E. (1994) Backbone dynamics of a free and phosphopeptide–complexed Src homology 2 domain studied by $^{15}$N NMR relaxation, *Biochemistry 33*, 5984–6003.
28. Wagner, G. (1983) Characterization of the distribution of internal motions in the basic pancreatic trypsin inhibitor using a large number of internal NMR probes., *Q. Rev. Biophysics 16*, 1–57.
29. Delaglio, F., Grzesiek, S., Vuister, G. W., Zhu, G., Pfeifer, J., and Bax, A. (1995)

NMRPipe: a multidimensional spectral processing system based on UNIX pipes, *Journal of Biomolecular NMR 6*, 277–293.

30. Vranken, W. F., Boucher, W., Stevens, T. J., Fogh, R. H., Pajon, A., Llinas, M., Ulrich, E. L., Markley, J. L., Ionides, J., and Laue, E. D. (2005) The CCPN data model for NMR spectroscopy: development of a software pipeline, *Proteins 59*, 687–696.
31. Shen, Y., Delaglio, F., Cornilescu, G., and Bax, A. (2009) TALOS+: a hybrid method for predicting protein backbone torsion angles from NMR chemical shifts, *Journal of Biomolecular NMR 44*, 213–223.
32. Cheung, M. S., Maguire, M. L., Stevens, T. J., and Broadhurst, R. W. (2010) DANGLE: A Bayesian inferential method for predicting protein backbone dihedral angles and secondary structure, *J Magn Reson 202*, 223–233.
33. Bax, A., Vuister, G. W., Grzesiek, S., Delaglio, F., Wang, A. C., Tschudin, R., and Zhu, G. (1994) Measurement of homo– and heteronuclear J couplings from quantitative J correlation, *Methods Enzymol 239*, 79–105.
34. Guntert, P. (1998) Structure calculation of biological macromolecules from NMR data, *Q Rev Biophys 31*, 145–237.
35. Brunger, A. T. (2007) Version 1.2 of the Crystallography and NMR system, *Nat Protoc 2*, 2728–2733.
36. Koradi, R., Billeter, M., and WÃ¼thrich, K. (1996) MOLMOL: a program for display and analysis of macromolecular structures, *Journal of molecular graphics 14*, 51–55.
37. Pettersen EF, Goddard TD, Huang CC, Couch GS, Greenblatt DM, Meng EC, and TE., F. (2004) UCSF Chimera–a visualization system for exploratory research and analysis. , *J Comput Chem. 13*, 1605–1612.
38. Kim, J. I., Ohtake, A., and Sato, K. (1997) Circular dichroism spectra of calcium channel antagonist omega–conotoxins, *Biochem Biophys Res Commun 230*, 133–135.
39. Fainzilber, M., van der Schors, R., Lodder, J. C., Li, K. W., Geraerts, W. P. M., and Kits, K. S. (1995) New Sodium Channel–Blocking Conotoxins Also Affect Calcium Currents in Lymnaea Neurons, *Biochemistry 34*, 5364–5371.
40. Imperial, J. S., Bansal, P. S., Alewood, P. F., Daly, N. L., Craik, D. J., Sporning, A., Terlau, H., Lopez–Vera, E., Bandyopadhyay, P. K., and Olivera, B. M. (2006) A novel conotoxin inhibitor of Kv1.6 channel and nAChR subtypes defines a new superfamily of conotoxins, *Biochemistry 45*, 8331–8340.
41. Sokolov, S., Kraus, R. L., Scheuer, T., and Catterall, W. A. (2008) Inhibition of Sodium Channel Gating by Trapping the Domain II Voltage Sensor with Protoxin II, *Molecular Pharmacology 73*, 1020–1028.
42. Favreau, P., Benoit, E., Hocking, H. G., Carlier, L., D' hoedt, D., Leipold, E., Markgraf, R., Schlumberger, S., Córdova, M. A., Gaertner, H., Paolini–Bertrand, M., Hartley, O., Tytgat, J., Heinemann, S. H., Bertrand, D., Boelens, R., Stöcklin, R., and Molgó, J. (2012) A novel μ–conopeptide, CnIIIC, exerts potent and preferential inhibition of NaV1.2/1.4 channels and blocks neuronal nicotinic acetylcholine receptors, *British Journal of Pharmacology 166*, 1654–1668.
43. Wittekind, M., and Mueller, L. (1993) HNCACB, a High–Sensitivity 3D NMR Experiment to Correlate Amide–Proton and Nitrogen Resonances with the Alpha– and Beta–Carbon Resonances in Proteins, *Journal of Magnetic Resonance, Series B 101*, 201–205.

44. Grzesiek, S., and Bax, A. (1993) Amino acid type determination in the sequential assignment procedure of uniformly $^{13}C$ / $^{15}N$–enriched proteins, *Journal of Biomolecular NMR 3*, 185–204.
45. Sharma, D., and Rajarathnam, K. (2000) $^{13}C$ NMR chemical shifts can predict disulfide bond formation, *Journal of Biomolecular NMR 18*, 165–171.
46. Johnson, C. E., and Bovey, F. A. (1958) Calculation of Nuclear Magnetic Resonance Spectra of Aromatic Hydrocarbons, *The Journal of Chemical Physics 29*, 1012–1014.
47. Dorman, D. E., and Bovey, F. A. (1973) Carbon–13 magnetic resonance spectroscopy. Spectrum of proline in oligopeptides, *The Journal of Organic Chemistry 38*, 2379–2383.
48. Pal, D., and Chakrabarti, P. (1999) Cis peptide bonds in proteins: residues involved, their conformations, interactions and locations1, *Journal of Molecular Biology 294*, 271–288.
49. Baker, E. N., and Hubbard, R. E. (1984) Hydrogen bonding in globular proteins, *Progress in Biophysics and Molecular Biology 44*, 97–179.
50. Jacob, R. B., and McDougal, O. M. (2010) The M–superfamily of conotoxins: a review, *Cell Mol Life Sci 67*, 17–27.
51. Han, Y. H., Wang, Q., Jiang, H., Liu, L., Xiao, C., Yuan, D. D., Shao, X. X., Dai, Q. Y., Cheng, J. S., and Chi, C. W. (2006) Characterization of novel M–superfamily conotoxins with new disulfide linkage, *FEBS J 273*, 4972–4982.
52. McDougal, O. M., and Poulter, C. D. (2004) Three–dimensional structure of the mini–M conotoxin mr3a, *Biochemistry 43*, 425–429.
53. Gupta, K., Kumar, M., and Balaram, P. (2010) Disulfide bond assignments by mass spectrometry of native natural peptides: cysteine pairing in disulfide bonded conotoxins, *Anal Chem 82*, 8313–8319.
54. Gray, W. R. (1993) Disulfide structures of highly bridged peptides: a new strategy for analysis, *Protein Sci 2*, 1732–1748.
55. Indu, S., Kochat, V., Thakurela, S., Ramakrishnan, C., and Varadarajan, R. (2010) Conformational analysis and design of cross–strand disulfides in antiparallel beta–sheets, *Proteins 79*, 244–260.
56. Ramachandran, G. N., Ramakrishnan, C., and Sasisekharan, V. (1963) Stereochemistry of polypeptide chain configurations, *J Mol Biol 7*, 95–99.
57. Laskowski, R. A., Rullmannn, J. A., MacArthur, M. W., Kaptein, R., and Thornton, J. M. (1996) AQUA and PROCHECK–NMR: programs for checking the quality of protein structures solved by NMR, *Journal of Biomolecular NMR 8*, 477–486.
58. Holm, L., and Rosenstrom, P. Dali server: conservation mapping in 3D, *Nucleic Acids Research 38*, W545–W549.
59. Akondi, K. B., Muttenthaler, M., Dutertre, S. b., Kaas, Q., Craik, D. J., Lewis, R. J., and Alewood, P. F. (2014) Discovery, Synthesis, and Structure–Activity Relationships of Conotoxins, *Chemical Reviews 114*, 5815–5847.
60. Wommack, A. J., Ziarek, J. J., Tomaras, J., Chileveru, H. R., Zhang, Y., Wagner, G., and Nolan, E. M. (2014) Discovery and characterization of a disulfide–locked c2–symmetric defensin Peptide, *J Am Chem Soc 136*, 13494–13497.
61. Miljanich, G. (2004) Ziconotide: neuronal calcium channel blocker for treating severe chronic pain, *Current medicinal chemistry 11*, 3029–3040.

62. Wishart, D. S., and Sykes, B. D. (1994) The $^{13}$C Chemical–Shift Index: A simple method for the identification of protein secondary structure using $^{13}$C chemical–shift data., *J. Biomol. NMR. 4*, 171–180.

## Tables

**Table 1 NMR and refinement statistics for protein structures**

| | |
|---|---|
| **NMR distance and dihedral constraints** | |
| Distance constraints | |
| Total NOE[a] | 547 |
| Intra–residue | 236 |
| Inter–residue | |
| Sequential ($\|i-j\|=1$) | 127 |
| Medium–range ($\|i-j\|\leq 4$) | 38 |
| Long–range ($\|i-j\|\geq 5$) | 146 |
| Hydrogen bonds[b] | 28 |
| Disulfide bond restraints[c] | 9 |
| Total dihedral angle restraints | |
| $\phi$ | 32 |
| $\psi$ | 35 |
| $\chi^{1}$[d] | 18 |
| $\omega$ | 1 |
| **Structure statistics**[e] | |
| Violations (mean and s.d.) | |
| Distance constraints (Å) | 0.00081 ± 0.0079 |
| Dihedral angle constraints (º) | 0.13997 ± 0.51906 |
| Max. dihedral angle violation (º) | 4.891 |
| Max. distance constraint violation (Å) | 0.188 |
| Deviations from idealized geometry | |
| Bond lengths (Å) | 0.018 |
| Bond angles (º) | 1.3 |
| Average pairwise r.m.s. deviation[f] (Å) | |
| Heavy | 1.18 ± 0.16 |
| Backbone | 0.68 ± 0.18 |

[a] Number of non–redundant and non–trivial NOE distance restraints
[b] Two distance restraints (acceptor oxygen to donor hydrogen and nitrogen) were included for each hydrogen bond that was observed in the long range HNCO experiment. [c] Three distance restraints (Cβ–Sγ', Sγ–Sγ' and Sγ–Cβ') were included for each disulfide bond. [d] $\chi^{1}$ restraints were obtained experimentally using 3D–HNHB and HN(CO)HB.
[e] Structure statistics were obtained using the protein structure validation server PSVS (http://psvs–1_5–dev.nesg.org/) [f] Pairwise r.m.s. deviation was calculated among 20 refined structures for the residues 3 to 36 using MOLMOL.

Figure Legends

Figure 1 : (a) Reverse Phase HPLC chromatograph of purified Mo3964. (b) LC–ESI–MS mass spectrum of purified Mo3964. The observed mass matches that of the oxidized peptide. (c) Far UV circular dichroism spectra of Mo3964 in oxidized and reduced conditions. (d) Fluorescence emission spectra of Mo3964 in oxidized and reduced conditions (with and without denaturants). (e) Refractive Index, Light Scatter ( 90° ) and UV detector (280 nm) signals along with molar mass of Mo3964 calculated by deconvolution of the Multi Angle Light Scattering data. (f) Residue–wise rotation correlation time calculated using $^{15}N$–relaxation data.

Figure 2: Electrophysiological studies.

(a) Reduction of whole–cell outward currents in rat DRG neurons by Mo3964 at 10 nM concentration. Plots (i) – (iv) are representative data from a single DRG neuron. (i) Family of mixed inward and outward currents elicited by depolarizing voltage steps from –65 to +25 mV in 10 mV steps from a holding potential of –80 mV. (ii) Reduction of outward currents by Mo3964 when applied to the bath. (iii) Mixed current traces at potential steps of 0 and 25 mV to show the preferential reduction, by Mo3964, of the outward current component measured 20 ms after pulse onset. (iv) Current–Voltage relationship shows the voltage dependent decrease of the outward current component. (v) Bar diagram showing reduction in mean current amplitude at the potentials indicated, after application of Mo3964 in bath. Each symbol represents data from a different cell (n=9). Error bars represent s.e.m. A two–tailed, paired t–test yielded a statistical significance of $p < 0.0001$ for the observed data (n=9).

(b) Modulation of rat brain type IIA voltage gated sodium channel α–subunit ($rNa_v1.2a$) by 10

nM Mo3964 (i) Representative leak and capacitance subtracted family of sodium current traces obtained in response to voltage steps from –60 to +100 mV (holding potential, –80 mV). (ii) Recordings from the same cell as in (i) after application of Mo3964. (iii) Normalized peak $I_{Na}$ vs membrane potential showing rightward shift in reversal potential (indicated by arrows) after the application of Mo3964. (iv) Normalized Conductance vs Membrane potential showing leftward shift in the presence of Mo3964. The data was fit with the Boltzmann charge–voltage equation. (v) Histogram showing change in mean reversal potential after application of Mo3964 in bath. The different symbols represent data from different cells. The error bars represent s.e.m. A two–tailed, paired t–test yielded a statistical significance of $p < 0.05$ for the observed data (n=7) . Data points are mean ± s.e.m (n = 7 )

Figure 3: (a) Sequence specifically assigned 2D–$^{1}H,^{15}N$–HSQC spectrum acquired at 600 MHz. A total of 56 well resolved correlation peaks (44 from backbone, 2 from side chain $HN^{\varepsilon}$–$N^{\varepsilon}$ of $Trp^{25}$, 4 from side chains of $Asn^{22, 36}$ and 6 from side chains of $Arg^{14, 33}$ ) were observed. Side–chain correlations are connected by horizontal dotted lines. The assignments for the minor peaks (5% in intensity when compared to the major form) are shown in red. (b) Strip plots from 3D–CBCA(CO)NH spectrum showing the $C^{\alpha}$ and $C^{\beta}$ correlations for the cysteine residues. (c) Carbon chemical shifts of proline residues seen in the 3D–CC(CO)NH ($Pro^{10}$, $Pro^{15}$ and $Pro^{24}$) and in the 3D–HCCH–COSY ($Pro^{37}$).

Figure 4: Strip plots from the 3D–HNHB (black) and 3D–HN(CO)HB (red) spectra. Missing and weak $H^{\beta}$ correlations are denoted by unfilled squares. Newman projections for the preferred side

chain $\chi^1$ conformations for cysteine residues are also shown.

Figure 5: Summary of the NMR data used for establishing the secondary structure in Mo3964 as a function of its amino acid sequence. Above the amino acid sequence, open and filled squares identify the residues whose backbone amide protons were protected up to 11 hours and 192 hours in H/D exchange study. The amide proton of $Lys^7$ was not observed in any of the conditions and is denoted by an asterisk. Below the amino acid sequence, filled circles represent residues with $^3J_{HNH\alpha} < 6$ Hz indicative of local helical conformation; open circles represent residues with $^3J_{HNH\alpha} > 8$ Hz indicative of residues in extended conformation; crosses represent residues with $^3J_{HNH\alpha}$ values between 6.0 to 8.0 Hz indicative of loop like conformation. For the sequential proton–proton NOE connectivities, $d_{\alpha N}$ , $d_{NN}$ and $d_{\beta N}$ ($d_{\alpha\delta}$ , $d_{N\delta}$ , and $d_{\beta\delta}$ for Xxx–Pro dipeptides, $d_{\alpha N}$ , $d_{\delta N}$ , and $d_{\beta N}$ for Pro–Xxx dipeptides), thick and thin bars indicate strong and weak NOE intensities, respectively. The observed medium–range NOEs $d_{\alpha N}$ (i,i+3 ), $d_{\alpha\beta}$ (i,i+3 ), $d_{\alpha N}$ (i,i+4 ), $d_{NN}$ (i,i+2 ), and $d_{\alpha N}$ (i,i+2 ) are indicated by lines connecting the two residues that are related by the NOE. The secondary chemical shift values of $^{13}C^{\alpha}$, $^{13}C^{\beta}$ and $^1H^{\alpha}$ are plotted at the bottom of the figure. Here, the positive values denote the chemical shifts which are down–field shifted when compared to the shifts in random coil values. The secondary chemical shifts of $C^{\beta}$ atoms of cysteine residues were calculated taking their oxidized state into consideration (*62*). The sequence locations of the five beta strands and the relative position of the six cysteines with respect to the strands are indicated schematically at the bottom of the figure. The figure is generated in part using the CcpNmr Analysis software(*30*).

Figure 6: (a) Assignment of inter–residue NOE correlations to $Trp^{25}$. (b) Strip plots from the long–range 3D–HNCO h–bond (Red) and a reference 3D–HNCO (black) spectra correlating

$^{h3}J_{NC'}$ scalar coupling across hydrogen bonds. (c) Schema showing long–range NOE and h–bond correlations. The inset shows the topology and the positions of cysteine residues (in yellow).

Figure 7: Disulfide connectivity by chemical cleavage. (a) RP–HPLC chromatogram of partially reduced and cyanylated Mo3964 indicating the fraction number and the corresponding masses detected. * denotes an impurity. (b) MALDI–MS mass spectra of the HPLC fractions 11 to 16a. (c) and (d) MALDI–MS mass spectra of singly reduced and cyanylated Mo3964 (fractions 14 to 16a) after chemical cleavage. The peptides with m/z 323.8 and 2845.5 indicate that $Cys^4$ and $Cys^{12}$ are disulfide paired. See text for details.

Figure 8: (a) On the left, topology of strands β2, β3, β4 and β5. The dot and cross in the top view denote the direction of strands coming out and going into the plane of the paper respectively. On the right, top views of the three possible disulfide pairings. Only the inter–sheet cross disulfide connectivity can explain the stability of Mo3964. (b) Stereo view of the superposed backbone heavy atoms (N, $C^{\alpha}$, C') and the cysteine side–chains (in red) of the 20 structures of Mo3964. (c) Ribbon representation of the lowest energy model of Mo3964. Secondary structure elements and residue numbers are labelled. Indicated on the figure are the side–chains of cysteines (in dark blue), the sulphur atoms (in yellow) and the disulfide bonds (in red). The disulfide linkage is depicted on the primary structure of Mo3964 at the bottom.

Figure 9: (a) Side and top views of Mo3964 showing the inter–sheet interactions. The side–chains of residues that point into the core of the structure are labeled in bold. The pairs of protons which exhibit NOE correlations are connected by broken blue lines. (b) Stick

representation of the side–chains of $Lys^{7}$, $Pro^{24}$ and $Trp^{25}$ which are involved in C-H•••π interactions. The centroids of the aromatic rings in the $Trp^{25}$ side–chain are shown by white spheres. The distances from ring–current shifted protons of $Lys^{7}$ and $Pro^{24}$ to the nearest centroid are shown. (c) One dimensional proton NMR spectrum of Mo3964 at pH 5.35 (50 mM $^{2}H_{3}$–acetate buffer). The insets show the overlay of spectral regions showing the down–field shifted amide protons and the up–field shifted aliphatic protons in native and denaturing conditions. The assigned peaks are labeled. The down–field shifted amide protons include those which are involved in the inter–strand hydrogen bonds (**cf Fig. 6c**) and the up–field shifted aliphatic protons are those which are involved in CH•••π interactions. The observation that the spectral dispersion in these regions is unaffected in the presence of high concentrations of Urea and Guanidinium chloride indicates that the inter–strand hydrogen bonds and the CH•••π interactions are unperturbed by these denaturants.

Figure 1

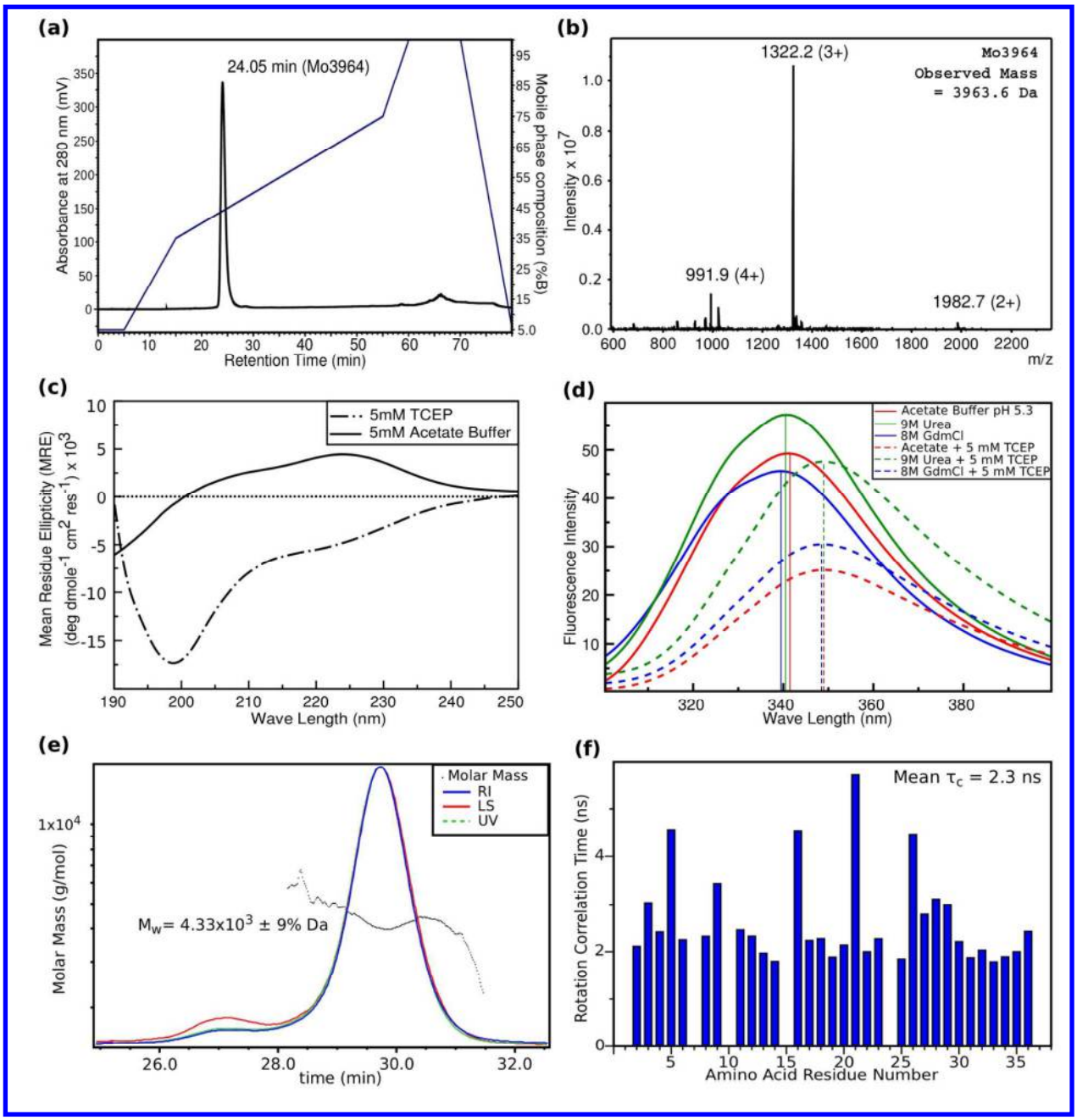
(a)
24.05 min (Mo3964)
Absorbance at 280 nm (mV)
Mobile phase composition (%B)
Retention Time (min)
(b)
1322.2 (3+)
Mo3964
Observed Mass
= 3963.6 Da
991.9 (4+)
1982.7 (2+)
Intensity x 10^7
m/z
(c)
5mM TCEP
5mM Acetate Buffer
Mean Residue Ellipticity (MRE)
(deg dmole^-1 cm^2 res^-1) x 10^3
Wave Length (nm)
(d)
Acetate Buffer pH 5.3
9M Urea
8M GdmCl
Acetate + 5 mM TCEP
9M Urea + 5 mM TCEP
8M GdmCl + 5 mM TCEP
Fluorescence Intensity
Wave Length (nm)
(e)
Molar Mass
RI
LS
UV
1x10^4
Molar Mass (g/mol)
Mw= 4.33x10^3 ± 9% Da
time (min)
(f)
Mean τc = 2.3 ns
Rotation Correlation Time (ns)
Amino Acid Residue Number

Figure 2a

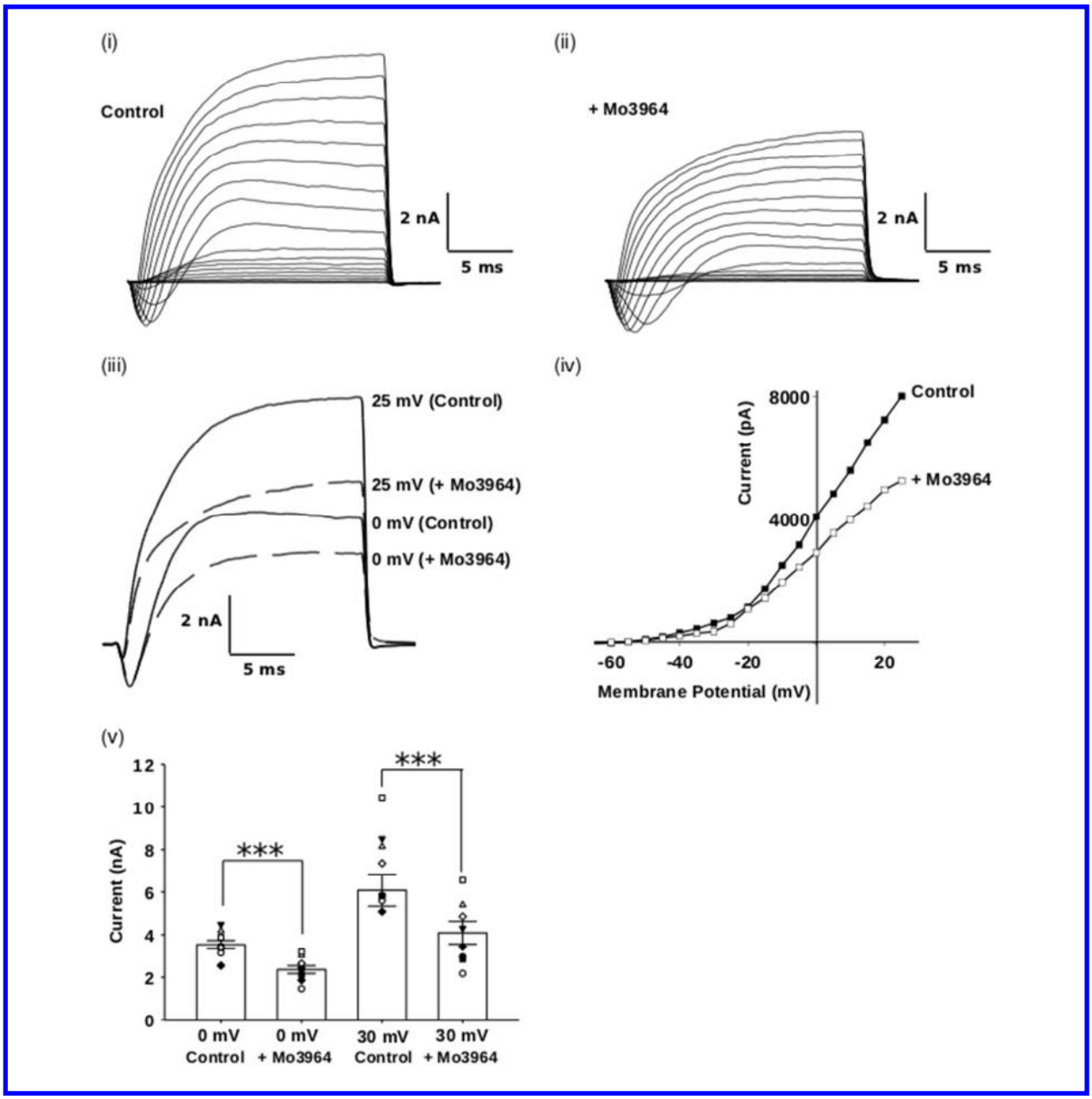
(i)
Control
2 nA
5 ms
(ii)
+ Mo3964
2 nA
5 ms
(iii)
25 mV (Control)
25 mV (+ Mo3964)
0 mV (Control)
0 mV (+ Mo3964)
2 nA
5 ms
(iv)
8000
4000
Current (pA)
Control
+ Mo3964
-60
-40
-20
20
Membrane Potential (mV)
(v)
12
10
8
6
4
2
0
Current (nA)
***
***
0 mV Control
0 mV + Mo3964
30 mV Control
30 mV + Mo3964

Figure 2b

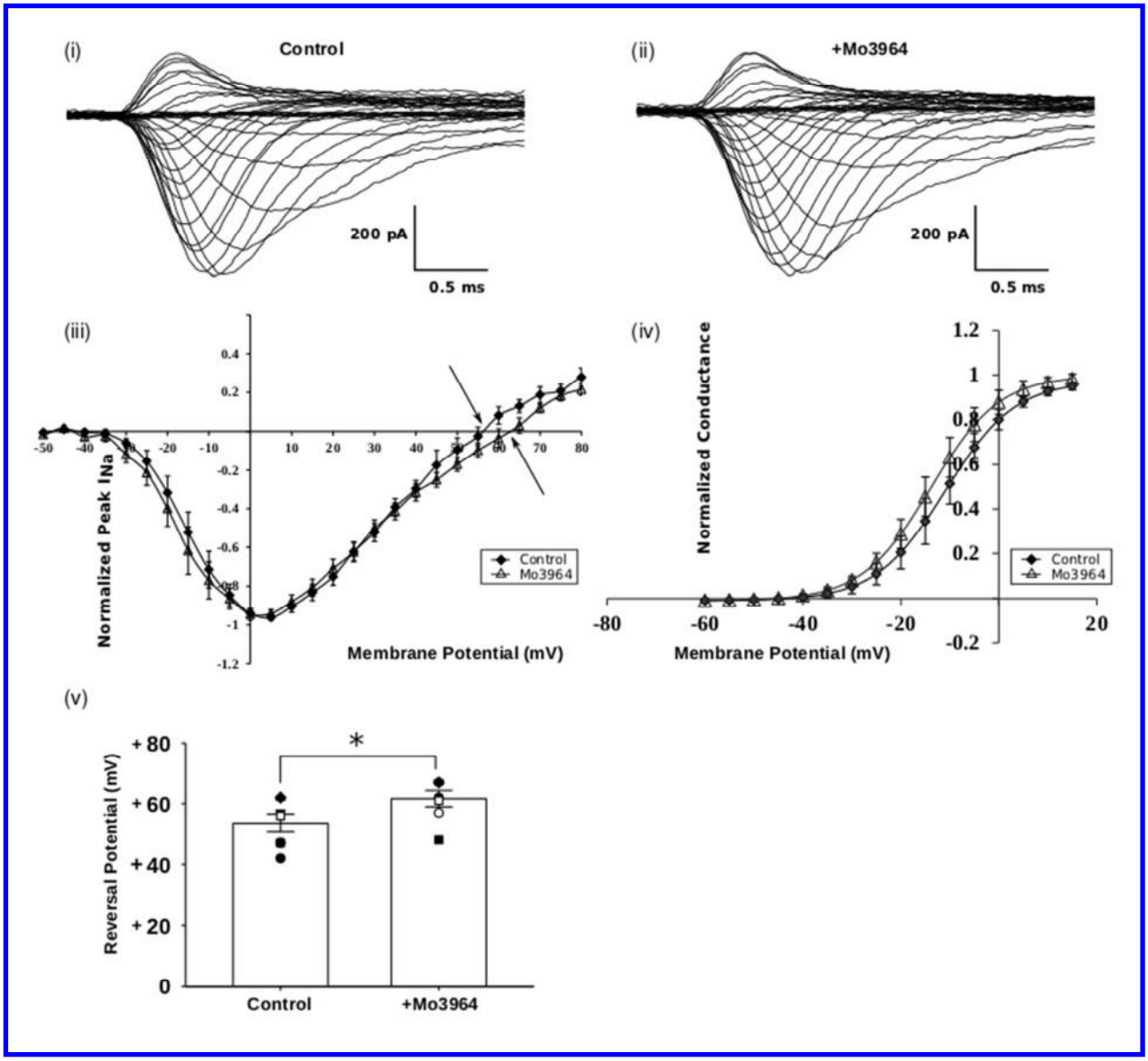
(i)
Control
200 pA
0.5 ms
(ii)
+Mo3964
200 pA
0.5 ms
(iii)
Normalized Peak INa
Membrane Potential (mV)
Control
Mo3964
(iv)
Normalized Conductance
Membrane Potential (mV)
Control
Mo3964
(v)
Reversal Potential (mV)
+80
+60
+40
+20
0
*
Control
+Mo3964

Figure 3

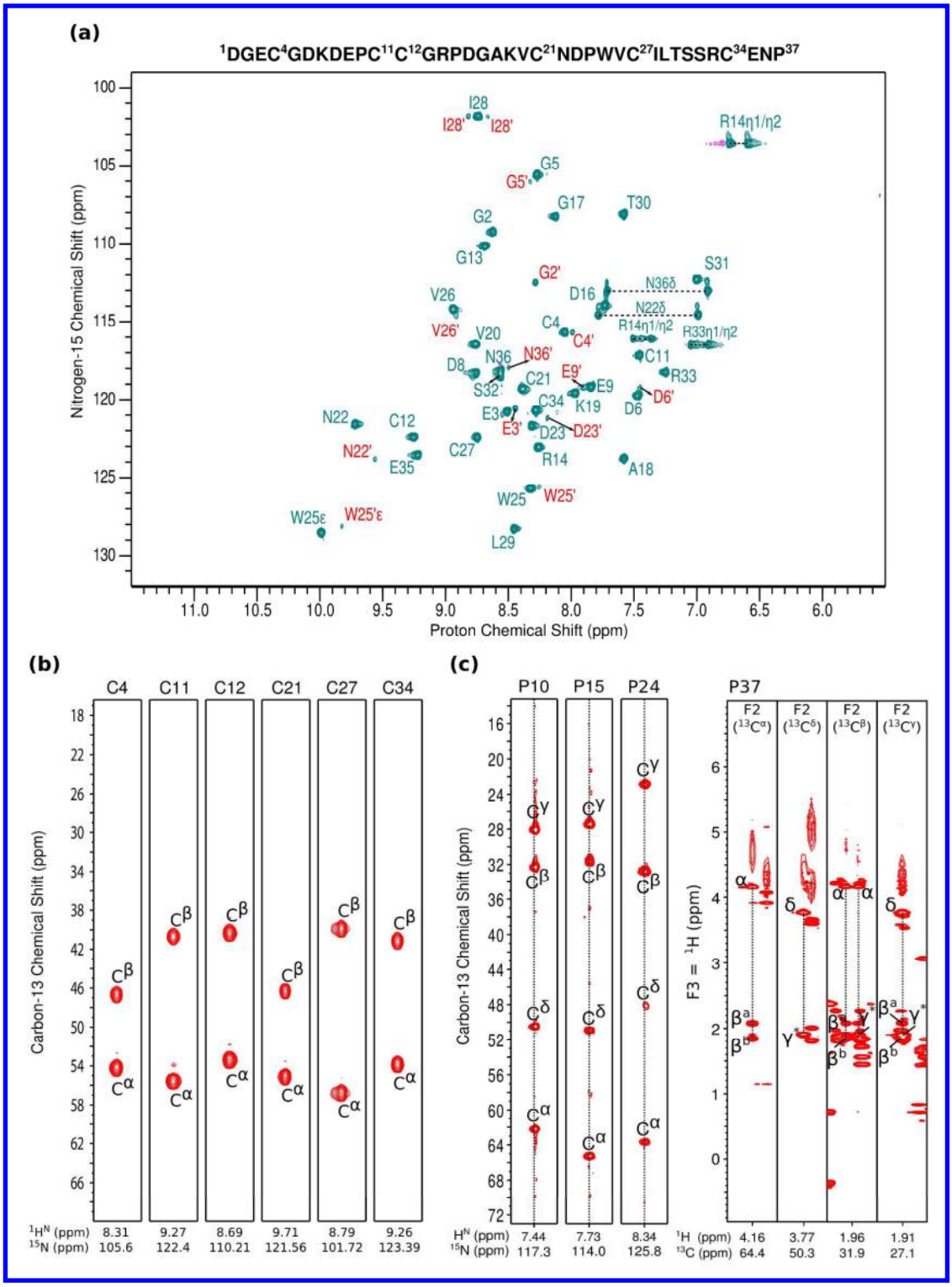
(a)
1DGEC4GDKDEPC11C12GRPDGAKVC21NDPWVC27ILTSSRC34ENP37
Nitrogen-15 Chemical Shift (ppm)
Proton Chemical Shift (ppm)
I28
I28'
R14η1/η2
G5
G5'
G17
T30
G2
G13
G2'
S31
N36δ
V26
D16
N22δ
V26'
V20
C4
C4'
R14η1/η2
R33η1/η2
N36
N36'
C11
D8
E9'
R33
C21
E9
S32'
C34
K19
D6
D6'
E3
N22
C12
E3'
D23
D23'
N22'
C27
R14
E35
A18
W25
W25'
W25ε
W25'ε
L29
(b)
C4
C11
C12
C21
C27
C34
Carbon-13 Chemical Shift (ppm)
1HN (ppm) 8.31 9.27 8.69 9.71 8.79 9.26
15N (ppm) 105.6 122.4 110.21 121.56 101.72 123.39
(c)
P10
P15
P24
P37
Carbon-13 Chemical Shift (ppm)
F2 (13Cα)
F2 (13Cδ)
F2 (13Cβ)
F2 (13Cγ)
F3 = 1H (ppm)
HN (ppm) 7.44 7.73 8.34
15N (ppm) 117.3 114.0 125.8
1H (ppm) 4.16 3.77 1.96 1.91
13C (ppm) 64.4 50.3 31.9 27.1

Figure 4

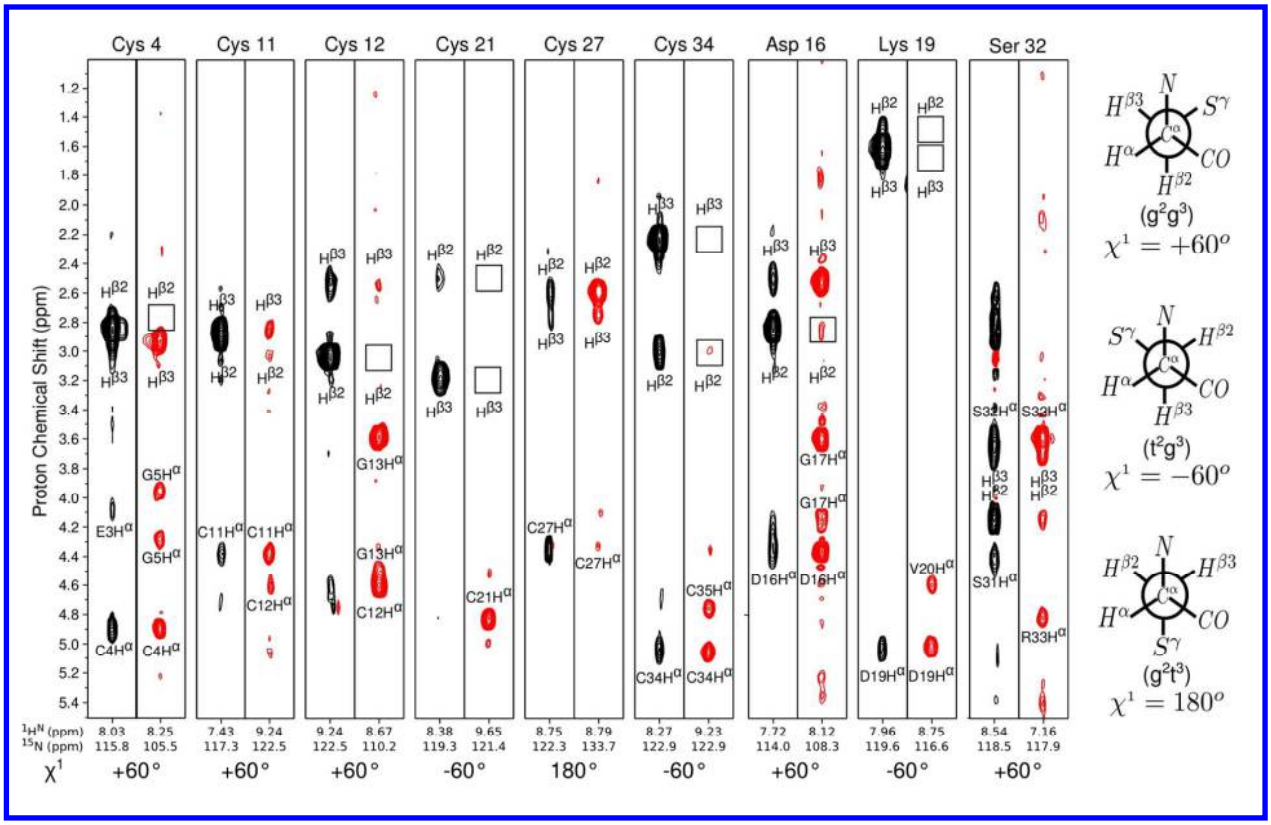
Cys 4
Cys 11
Cys 12
Cys 21
Cys 27
Cys 34
Asp 16
Lys 19
Ser 32
Proton Chemical Shift (ppm)
χ1
+60°
+60°
+60°
-60°
180°
-60°
+60°
-60°
+60°
(g2g3)
χ1 = +60o
(t2g3)
χ1 = −60o
(g2t3)
χ1 = 180o

Figure 5

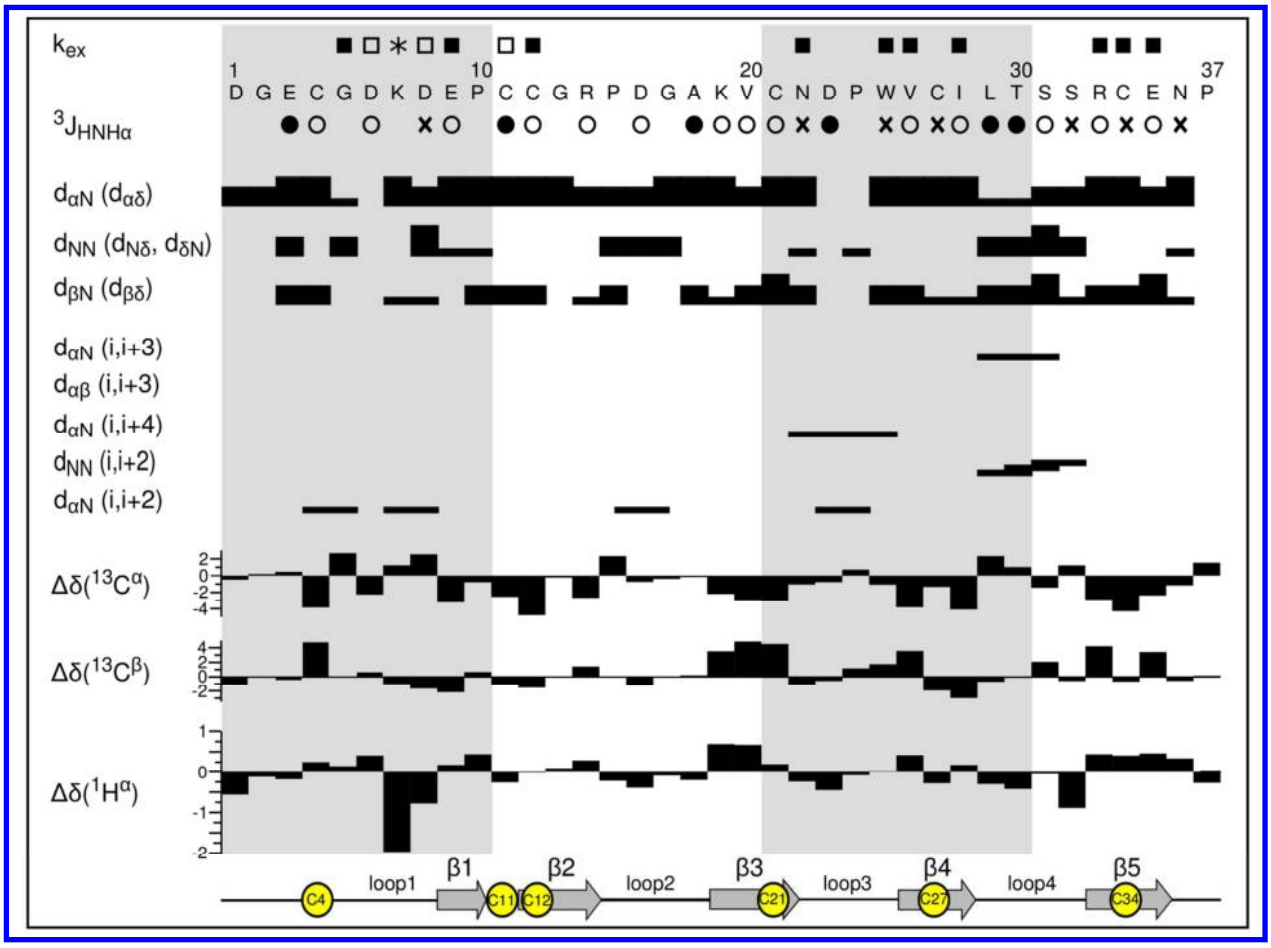
kex
1
10
20
30
37
D G E C G D K D E P C C G R P D G A K V C N D P W V C I L T S S R C E N P
3JHNHα
dαN (dαδ)
dNN (dNδ, dδN)
dβN (dβδ)
dαN (i,i+3)
dαβ (i,i+3)
dαN (i,i+4)
dNN (i,i+2)
dαN (i,i+2)
Δδ(13Cα)
Δδ(13Cβ)
Δδ(1Hα)
β1
β2
β3
β4
β5
loop1
loop2
loop3
loop4
C4
C11
C12
C21
C27
C34

Figure 6

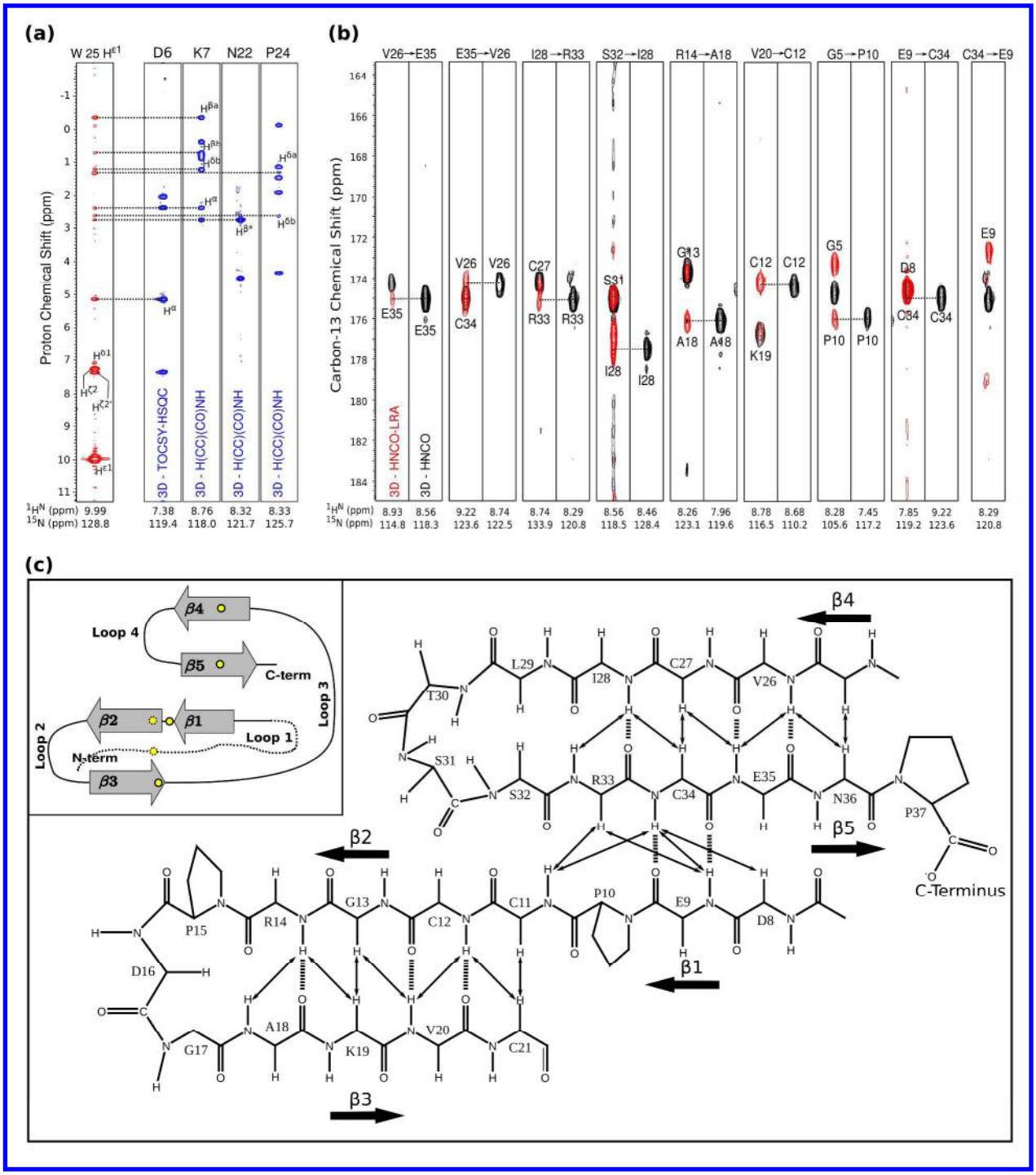
(a)
W 25 Hε1
D6
K7
N22
P24
Proton Chemical Shift (ppm)
3D - TOCSY-HSQC
3D - H(CC)(CO)NH
3D - H(CC)(CO)NH
3D - H(CC)(CO)NH
(b)
V26→E35
E35→V26
I28→R33
S32→I28
R14→A18
V20→C12
G5→P10
E9→C34
C34→E9
Carbon-13 Chemical Shift (ppm)
3D - HNCO-LRA
3D - HNCO
(c)
Loop 4
β4
β5
C-term
Loop 3
β2
β1
Loop 2
Loop 1
N-term
β3
C-Terminus

Figure 7

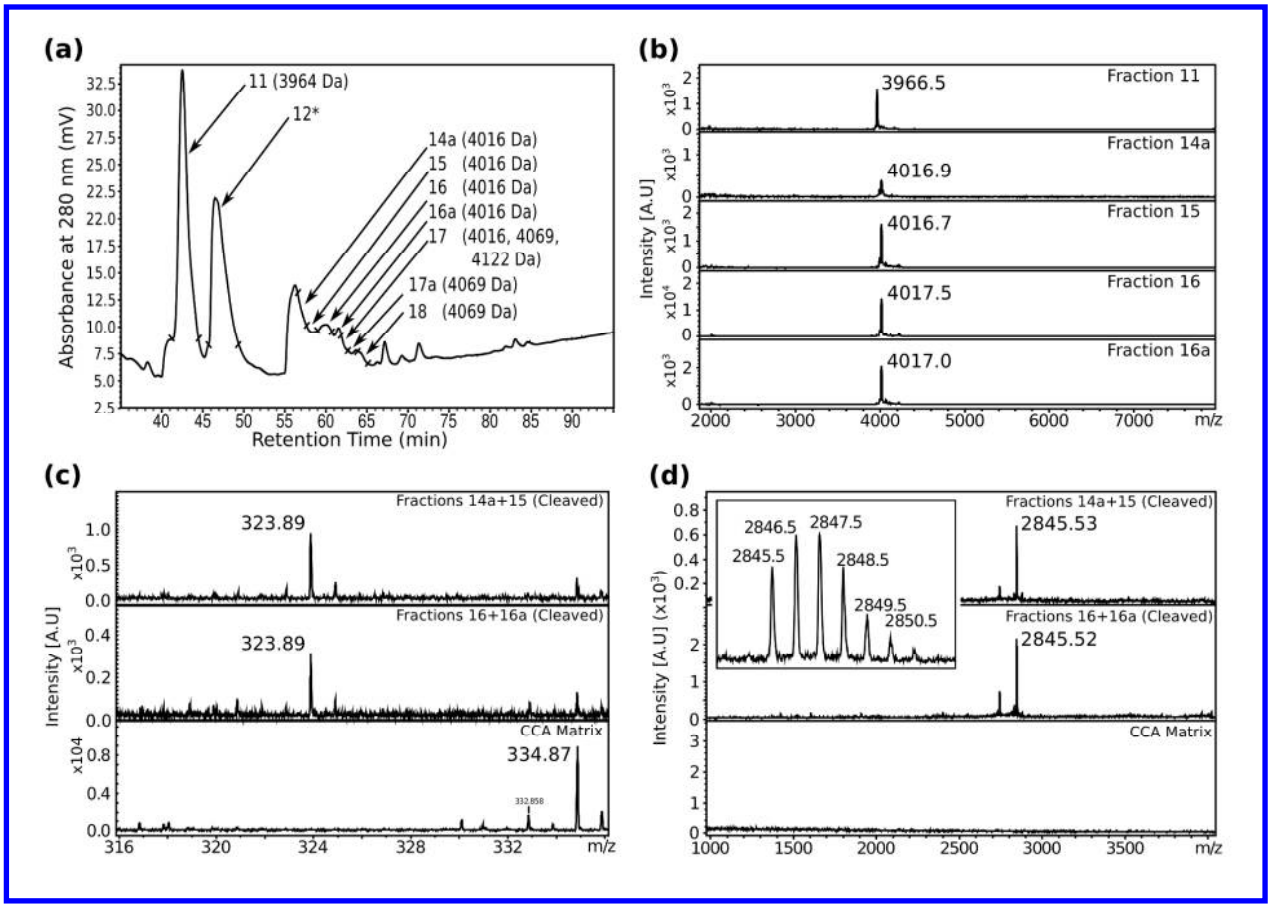
(a)
Absorbance at 280 nm (mV)
Retention Time (min)
11 (3964 Da)
12*
14a (4016 Da)
15 (4016 Da)
16 (4016 Da)
16a (4016 Da)
17 (4016, 4069, 4122 Da)
17a (4069 Da)
18 (4069 Da)
(b)
Intensity [A.U]
Fraction 11
3966.5
Fraction 14a
4016.9
Fraction 15
4016.7
Fraction 16
4017.5
Fraction 16a
4017.0
m/z
(c)
Intensity [A.U]
Fractions 14a+15 (Cleaved)
323.89
Fractions 16+16a (Cleaved)
323.89
CCA Matrix
334.87
m/z
(d)
Intensity [A.U] (x10³)
Fractions 14a+15 (Cleaved)
2845.53
2846.5
2847.5
2845.5
2848.5
2849.5
2850.5
Fractions 16+16a (Cleaved)
2845.52
CCA Matrix
m/z

801 Figure 8

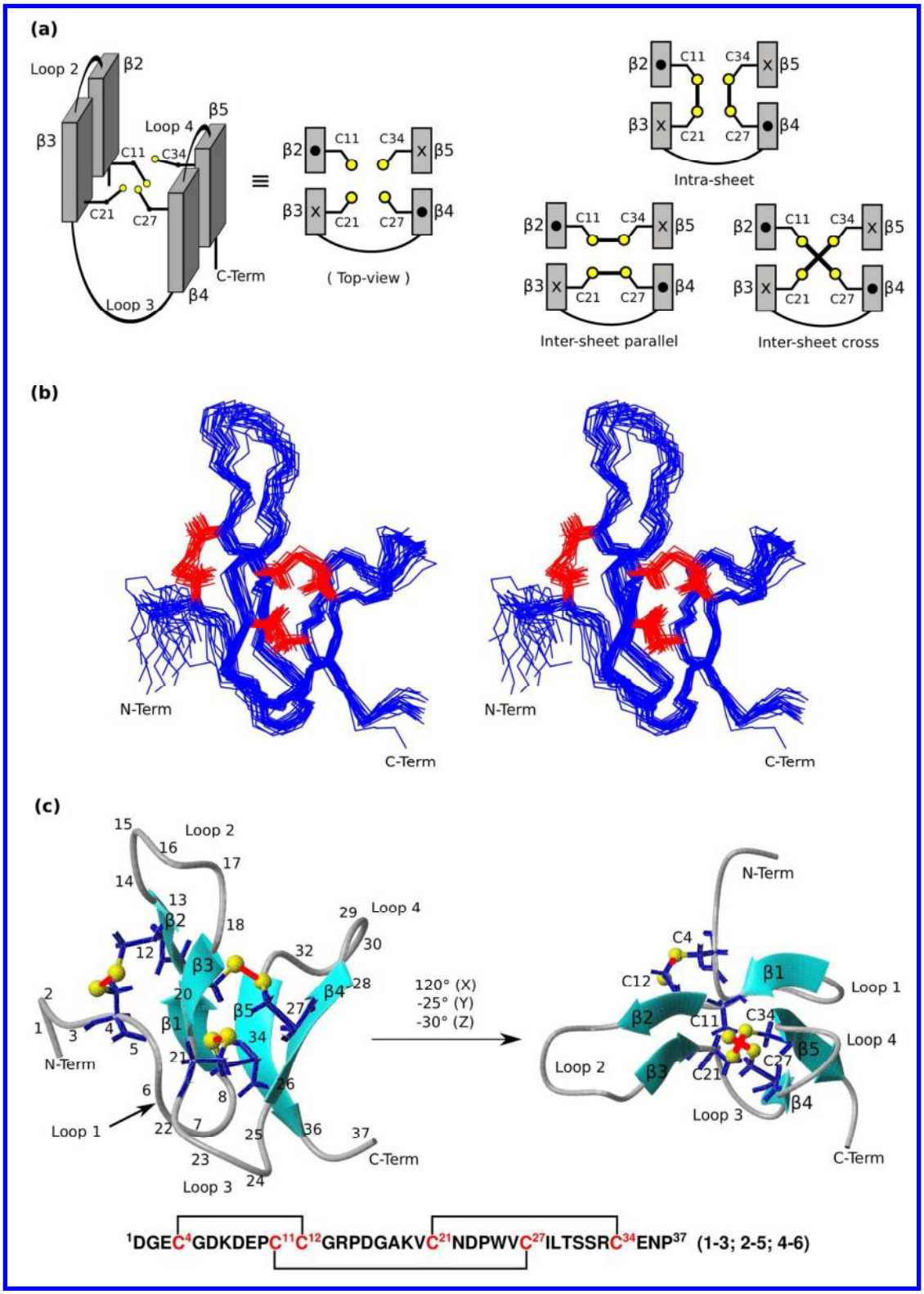
(a)
Loop 2
β2
β3
Loop 4
β5
C11
C34
C21
C27
C-Term
Loop 3
β4
≡
( Top-view )
Intra-sheet
Inter-sheet parallel
Inter-sheet cross
(b)
N-Term
C-Term
(c)
Loop 2
Loop 4
Loop 1
Loop 3
N-Term
C-Term
120° (X)
-25° (Y)
-30° (Z)
C4
C12
C11
C34
C21
C27
¹DGEC⁴GDKDEPC¹¹C¹²GRPDGAKVC²¹NDPWVC²⁷ILTSSRC³⁴ENP³⁷ (1-3; 2-5; 4-6)

802 Figure 9

803

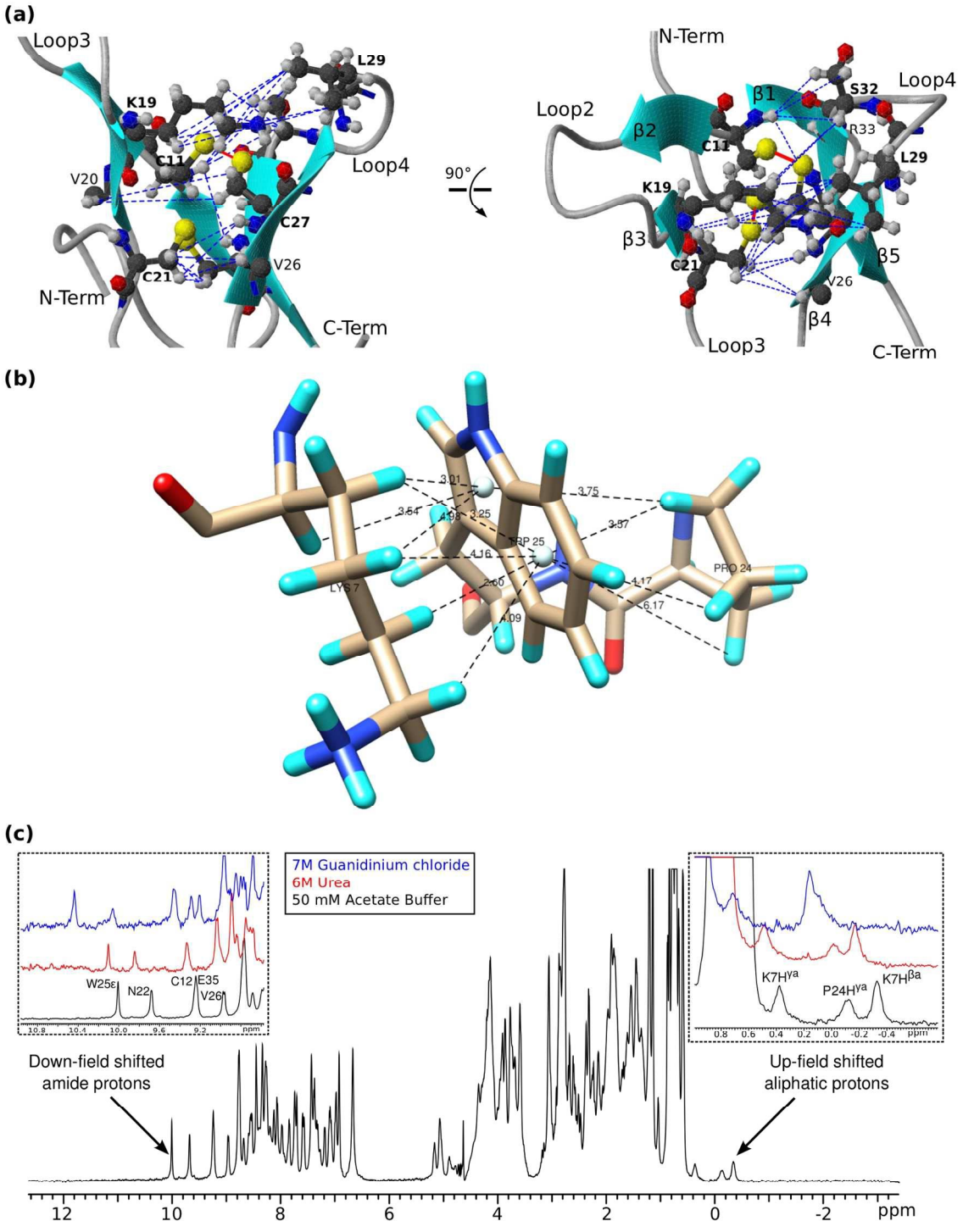

Table of Contents Graphic